AIAA JOURNAL
Vol. 47, No. 6, June 2009

Exploitation of Higher-Order Membrane Modes for Improved Synthetic Jet Performance

Geoff A. Slipher* and James E. Hubbard Jr.†
University of Maryland, College Park, Maryland 20742

DOI: 10.2514/1.36886

Electroactive polymer synthetic jets (E-jets) are a new lightweight low-power means of generating a synthetic jet for low-speed active flow control applications. The actuation method uses a thin (≈30 μm) prestrained low modulus and a circular-composite-dielectric acrylic elastomer membrane. The membrane is excited to operate at transverse resonance to pump air in and out of a partially closed chamber. Based on device configurations experimentally tested to date, the attainable nozzle velocity has been determined to be greater than 25 m/s at a nozzle exit diameter of 13 mm and a frequency of approximately 250 Hz *without optimization*. While performing device frequency sweep characterization, it was noted that certain higher membrane vibration modes induced significantly greater jet velocities than the fundamental membrane mode. A series of tests was performed using a stroboscope to identify the modes and correlate them qualitatively with device performance. These tests verified the presence of classical membrane modes. A second series of tests was then performed using a scanning laser vibrometer to quantitatively correlate membrane mode shapes with device performance. The vibrometer tests experimentally attributed peak velocity performance to the presence of one particular nonclassical higher-order mode. The exploitation of coupled higher-order membrane modes for increased synthetic jet performance represents a new operating paradigm for similar classes of systems.

I. Introduction

FOR more than a decade, significant effort has been applied to studying and developing synthetic jet actuators for active flow control applications [1]. Motivational factors influencing this effort include increasingly stringent demands for reducing vehicle emissions, reducing vehicle acoustic loads, and reducing vehicle drag while increasing vehicle capabilities such as cargo capacities, aircraft short takeoff and landing capabilities, endurance, and range.

Flow control, broadly defined, refers to the intentional manipulation of a flowfield to induce desired flow phenomena in the presence of specific flow conditions. This may include passive or active flow control, in which passive control solutions are typically aimed at a narrow design point (e.g., cruise speed), and active flow control solutions tend to be more broadband in terms of applicability. Active control implies some adaptability in how and when a given solution is to be applied, which thus adds a requirement for a feedback mechanism and control algorithm for implementation.

There is currently a large body of literature discussing active flow control techniques and strategies [2–4], and so the authors deem it unnecessary to summarize the field in detail. The authors do, however, emphasize two active flow control techniques that relate to the specific issues of synthetic jet actuator characterization discussed in this paper: 1) circulation control and 2) boundary-layer separation control. Circulation control involves operating a synthetic jet device in an attached-flow regime at relatively high frequencies and a sufficient jet-to-freestream velocity ratio to produce recirculation regions of flow that can be used to change the shape of the aerodynamic body in a virtual way, thereby actively altering distribution of the aerodynamic loading [5]. On the other hand, boundary-layer separation control, the origins of which can be traced all the way back to the infancy of heavier-than-air flight [6], involves relatively low-frequency actuation of a synthetic jet ahead of an aerodynamic surface experiencing separation to delay that separation from occurring [7].

In the open literature, synthetic jets are most often described in terms of two functional parameters: 1) frequency of operation and 2) induced velocity at the nozzle exit. Two equations are used most often to relate these functional parameters to potential flow control applications. The first such equation relates the so-called momentum coefficient C_μ [8]:

$$C_\mu = \frac{2\rho_j U_j^2 b}{\rho U^2 c} \tag{1}$$

where ρ and ρ_j are the freestream and jet fluid densities, U_j is the averaged jet velocity at the nozzle exit, U is the freestream velocity, c is an application-specific geometric parameter describing a characteristic length to be influenced by the synthetic jet (e.g., wing chord length), and b is a geometric parameter describing the actuator geometry, typically the width or diameter of the actuator's nozzle. For adequate control authority in flow separation control applications, the momentum coefficient must be, at a minimum, on the order of 10e-3 [9]. The beneficial effect that an increasing jet momentum coefficient has on reattaching the boundary layer was described by McCormick [9].

The second archetypal equation used to relate synthetic jet performance applicability is the nondimensional frequency parameter F^+ [10]:

$$F^+ = \frac{f_j c}{U} \tag{2}$$

where f_j is the frequency at which the synthetic jet is actuated, and U and c remain the same as in the equation for the momentum coefficient. When considering the nondimensional frequency as it relates to active flow control, there are currently two known acceptable regimes of operation: 1) $F^+ \approx 1$ [1,11], and 2) $F^+ \approx 10$ [12].

Understanding the relationship between actuation frequency and induced jet velocity is critical to understanding how a given synthetic jet actuator may be used in a real application. Thus, the motivation for a study of membrane modal correlation with device performance is clear, given that velocity performance of the actuator scheme

Presented as Paper 284 at the 46th Annual Aerospace Sciences Meeting, Reno, NV, 7–10 January 2008; received 28 January 2008; revision received 4 March 2009; accepted for publication 6 March 2009.

*Graduate Research Assistant, Department of Aerospace Engineering; slipherg@umd.edu. Student Member AIAA.

†Samuel P. Langley Professor, Department of Aerospace Engineering. Associate Fellow AIAA.

discussed in this paper has been determined to be highly dependent on membrane dynamics (in particular, mode shape), which is in turn highly frequency-dependent.

It was previously reported by Gilarranz et al. [13] that a synthetic jet actuation mechanism with a peak-to-peak stroke amplitude "on the order of 5 mm at a frequency around 300 Hz would be optimal for real-life flight applications." The authors pointed out that such a deflection-bandwidth relation is not appropriate for piezoceramics, but that it is in fact appropriate for actuation with electric motors, the actuation scheme they were researching. The deflection-bandwidth characteristics for the composite diaphragm presented in this paper closely match these numbers for real-life flight applications and thus provide a new, mechanically simple, lightweight, and low-power alternative to piezoceramic and electromagnetically driven synthetic jet designs. The device incorporating this new actuation scheme is referred to by the authors as an electroactive polymer synthetic jet, or E-jet.

Table 1 shows a comparison of synthetic jet actuator performance as reported in the available open literature. It is difficult to compare across all metrics, because not all research programs have consistently reported the same data, due to each program having varying objectives and purposes. Nevertheless, the table gives some idea of the range of available synthetic jet actuator designs and their relative characteristics. It is clear from the table that the E-jet's acrylic dielectric elastomer diaphragm affords it a unique niche in the range of available synthetic jet options for low-speed active flow control.

Table 1 clearly shows that the E-jet has a low-frequency, high-displacement active mechanism that generates reasonable jet velocities in a compact, lightweight, and low-power form factor. It is worth emphasizing that although the E-jet actuation mechanism requires a high voltage, it requires small amounts of power to drive it, allowing for compact and lightweight power supplies to be used. The E-jet is also easily scalable.

The experimental observations of membrane behavior described in this paper represent a new contribution to experimental membrane dynamic studies. Although the study of membrane vibrations may be traced back more than three centuries, and dozens of papers on theoretical membrane analysis may be found in the literature, only a small number of experimental membrane studies are currently available [22]. These results thus represent an important contribution to the experimental study of membrane dynamics and can be used to inform future membrane modeling efforts.

This work also represents the first known study to report a distinct increase in synthetic jet performance by employing membrane structural dynamics higher than the fundamental. All known preceding papers [18,23–35] that address the performance of synthetic jets employing the ubiquitous circular or rectangular diaphragm have focused analysis and experimental assessment on the first membrane mode or have approximated it as a piston. It is intuitive that the first membrane mode would give the best performance in similar cases, due to it having the highest net displacement and thus moving the largest volume of air. However, what makes the results presented in this paper distinctly different from prior works is that the first membrane mode does not give the best performance, thus presenting a new and nonintuitive result.

For the highly nonlinear E-jet system, a higher-order mode provides dramatically better performance over the fundamental. What will be of particular interest to other researchers is that the demonstrated and significant improvement in performance that using higher-order modes brings in this particular type of system may be applicable to their own similar devices as well as to other new actuation schemes. The result also has a significant impact on assumptions that go into future efforts to model the E-jet device. The advantage of using higher-order modes for this type of system exists due to the improvement in performance that is gained by matching the diaphragm, chamber, and nozzle subsystem impedances. The concept of exploiting higher-order modes to gain increases in membrane-driven synthetic jet performance may be applicable to other synthetic jet designs and, as such, represents a new operating paradigm for similar classes of systems with low-mechanical-impedance driving mechanisms.

The remainder of this paper describes the device and the experimental techniques employed to study it and discusses the dynamic operating characteristics of this new mechanism for actuating a synthetic jet: a resonating electroactive polymer composite diaphragm.

II. E-Jet Device

The E-jet system is composed of three functional subsystems [36]: 1) the low-mechanical-impedance active composite diaphragm, 2) the resonant chamber, and 3) the nozzle, sometimes referred to in the literature as an orifice. Figure 1 shows that the device itself is assembled from three components: 1) the acrylic dielectric elastomer membrane, 2) the compliant electrode (including the electrical leads), which together comprise the active composite diaphragm subsystem, and 3) the rigid structure, which makes up both the chamber and nozzle subsystems.

A mechanically simple strategy for actuating a synthetic jet is to place a transversally vibrating membrane at one end of a partially enclosed chamber. As it vibrates, the membrane alters the chamber volume periodically, forcing the air in and out of the surrounding structure through a nozzle. E-jets employ just such a vibrating membrane for actuating the synthetic jet. Whereas previous synthetic jet designs have employed relatively stiff membranes (e.g., piezocrystal diaphragms) with small vibrational displacements at relatively high frequencies [3], E-jets are actuated using a low-elastic modulus elastomer that is operated at low frequency and large displacement to induce a sufficient jet velocity out of the nozzle. Thomas [37] recently compared the displacement, force, efficiency, and actuation frequency performance for a variety of actuation materials and strategies currently being researched or already in use. The E-jet employs an acrylic dielectric elastomer as the active material. This material, as described by Thomas [37], has a compromise of qualities that make it a useful candidate for application to the synthetic jet actuator design space for low-speed active flow control applications.

To vibrate the membrane, E-jets take advantage of a simple compliant capacitor actuation principle. A strong electric field is applied across the membrane thickness through compliant electrodes applied to opposing membrane surfaces. One side of the membrane acts as the cathode, and the other acts as the anode. Applying an electric field induces a pressure across the membrane thickness, known as Maxwell stress. This pressure acts to compress the membrane in the thickness direction in the area sandwiched by the electrodes. The induced pressure across the membrane thickness is related by the equation [38]

$$P = \varepsilon_r \varepsilon_0 E^2 = \varepsilon_r \varepsilon_0 \left(\frac{V}{t}\right)^2 \tag{3}$$

where ε_r is the dielectric constant of the elastomer membrane material, ε_0 is the relative permittivity of free space, E is the electric field strength, V is the applied voltage, and t is the thickness of the membrane material. Because the acrylic elastomer used in the testing (3M's VHB4905) has a Poisson's ratio very close to 0.5, it may be considered incompressible. Thus, the volume of the membrane material remains constant during actuation. Because of an applied membrane prestrain, the membrane is biased to expand in the x–y plane orthogonal to the applied electric field (z). Induced pressure in the membrane thickness direction decreases the membrane thickness, resulting in an expansion of the membrane area sandwiched by the electrodes. By simultaneously increasing the area of the membrane and reducing its thickness, the effective stiffness of the membrane is thus locally reduced in the area covered by the electrodes.

The elongation directions x and y are referred to in this paper as the directions of excitation. Figure 2 shows two photographs superimposed on one another. One photograph is taken with a 4000 V field applied (the larger-diameter shadow image), and one is taken with no field applied. The change in area covered by the electrode (black material) can be seen. Note that the membrane

Table 1 Comparison of zero-net mass-flux synthetic jet actuators from data reported in the open literature[a]

Mechanism	Frequency, Hz	Stroke	Velocity at nozzle	Power	Mass	Chamber shape	Chamber size	Nozzle shape	Nozzle size
2009 [14] (University of Florida), magnetically driven composite diaphragm	50–200 Hz	N/R	35 m/s	N/R	80 g	Cylinder	$D = 30$ mm; $L = 20$ mm	Cylinder	$D = 2$ mm; $L = 1$ mm
2007 [15] (University of Maryland), composite acrylic dielectric elastomer diaphragm	250 Hz	2 mm, typical peak displacement	25 m/s	0.4 W rms	<10 g	Cylinder	$D = 50.8$ mm; $L = 22.5$ mm	Cylinder	$D = 12.7$ mm; $L = 5.33$ mm
2007 [3] (University of Maryland), Thunder composite piezoceramic diaphragm	2200 Hz	0.065 mm	40 m/s	12 W	8 g	Cylinder	$D = 32$ mm; $L = 6.1$ mm	Cylinder	$D = 1.1$ mm; $L = 1.5$ mm
2006 [16] (University of Maryland), dual recurved piezoceramic composite diaphragms	145 Hz	1.1 mm	20 m/s	N/R	50 g	Rectangle	$L = 73.7$ mm; $W = 8.7$ mm; $H = 22.9$ mm	Rectangle	$L = 76.2$ mm; $W = 1.14$ mm
2005 [17](University of Washington), ferromagnetic shape memory alloy composite diaphragm	220 Hz	1 mm	190 m/s	100 W	1360 g	Cylinder (dual)	$D = 64$ mm; $L = $ N/R	Rectangle	$L = 5$ mm; $W = 1$ mm
2002 [13] (Texas A&M University), electric motor driven piston-cylinder	130 Hz	22 mm	90 m/s	135 W per piston (x6)	N/R	Rectangle	$L = 24.1$ mm; $W = 6.35$ mm; $H = 44.7$ mm	Rectangle	$L = 150$ mm; $W = 2$ mm
2001 [18] (U.S. Air Force Academy), piezoceramic composite diaphragm	700 Hz	N/R	8.7 m/s	N/R	N/R	Cylinder	$D = 30$ mm; $H = 2$ to 7.62 mm	Rectangle	$L = 30$ mm; $W = 0.5$ mm
2000 [9] (United Technologies Research Center), cavity pressure-speaker (voice coil)	50–200 Hz	N/R	7 to 23 m/s	2 to 50 W	N/R	N/R	N/R	Rectangle	$L \approx 500$ mm; $W = 6.4$ mm
2000 [19] (NASA Langley Research Center), dual piezoceramic composite diaphragms	400 Hz	0.5–1.0 mm	60 m/s	N/R	N/R	Cylinder	$D = 50$ mm; $L = $ N/R	Rectangle	$L = 35$ mm; $W = 0.5$ mm
2000 [20] (The Boeing Company), dual half-cylinder composite PVdF diaphragms	25 Hz	8.3 mm	7.2 m/s	N/R	N/R	Rectangle	$L = 75$ mm; $W = 25$ mm; $H = 19$ mm	Rectangle	$L = 19$ mm; $W = 0.75$ mm
1997 [21] (Georgia Institute of Technology), piezoceramic composite diaphragm	500–1000 Hz	N/R	25 m/s	N/R	N/R	Rectangle	$L = 76.2$ mm; $W = 12.7$ mm; $H = 710$ mm	Rectangle	$L = 75$ mm; $W = 0.5$ mm

[a]N/R indicates that the metric was not reported in the cited work.

material itself is transparent. In this particular image, a 21% change in area is achieved through a steady application of the electric field. Although the required operating voltage is high, the total power required during operation is low and is typically measured in tenths of a watt rms at maximum power consumption.

The membrane vibrations are excited using either a sinusoidal or square wave voltage signal at a resonant frequency, thus periodically varying the effective stiffness of the membrane. A dc bias is applied to the periodic excitation voltage signal to maintain a periodic voltage potential that is always positive. This dc bias is convenient

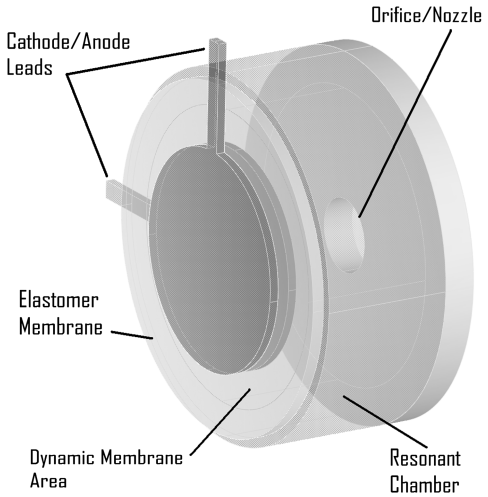

Fig. 1 E-jet device components and assembly diagram; membrane and electrode thicknesses are not shown to scale.

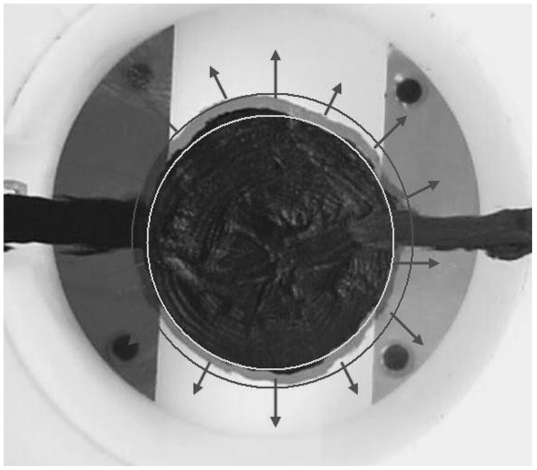

Fig. 2 Membrane excitation due to applied electric field.

because a pressure is generated by the electrodes regardless of the direction of the electric field potential, and an unbiased signal would therefore be exciting the membrane at twice the frequency of the input signal and at only $\frac{1}{2}$ the electric field strength. Figure 3 illustrates how the E-jet device operates using the resonating membrane to move air in and out of a chamber. It also shows how membrane actuation direction (i.e., the direction of vibration) is parallel to the direction of the applied electric field and thus transverse[‡] to the excitation direction.

When the electric field is applied periodically at a membrane resonant frequency, the effective stiffness of the membrane is cyclically altered at the same frequency. When this varying stiffness is combined with a self-induced out-of-plane perturbation, the membrane self-excites in a drum mode correlated with the frequency of excitation. Figure 4 shows an on–off–on sequence of membrane excitation at the resonant frequency of the first membrane mode shape (0,1). The figure is included to clarify the transverse nature of the membrane's vibratory displacement versus the excitation direction.

Once the resonant frequency excitation is introduced and is combined with the out-of-plane perturbation, the membrane system quickly attains a steady-state vibration. Experimental data representing the time history of this process are presented in Fig. 5,

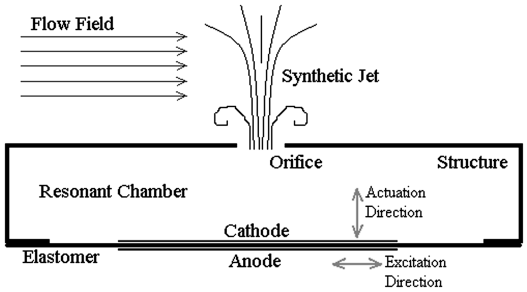

Fig. 3 Basic E-jet system diagram.

which indicates membrane displacement measured at a discrete offcenter point versus time.

Steady-state vibration is easily maintained by running the excitation signal continuously at the appropriate resonant frequency. Because the E-jet system is essentially a self-exciting drum, a drum harmonic series is considered for a baseline comparison rather than the more typical harmonic series.[§] Figure 6 shows the harmonic frequency spacing relative to the fundamental modal frequency (f_1) as well as the location of the diametral and circumferential nodes for classical axisymmetric membrane modes. It has been experimentally verified that any one of the classical membrane modes may be excited and maintained in the described manner up to and including membrane mode (4,1). It was difficult to experimentally verify the effective excitation of modes higher than (4,1), due to the tendency of the thin membranes to tear and due to occasional destructive electrode arcing effects that increase in likelihood with increased strain gradients across the membrane and electrode surfaces.

III. Experiment

The membrane material used in these experiments was a self-adhesive 3M elastomer known as VHB4905. The elastomer was biaxially prestrained 100% by 100% in the x and y directions to bias its actuation and was then mounted to a rigid frame. Prestraining the elastomer has additional beneficial and detrimental effects described by Choi et al. [39]. A thin layer of compliant electrode material composed of a carbon suspension in silicon oil combined with a thickening agent was equally applied to both sides of the membrane. Simple holes of various diameters were drilled in stiff plastic plates of varying thicknesses to form the different chamber nozzles. Figure 7 shows the basic experiment layout used to measure E-jet performance.

For the experiments discussed in this paper, membranes were manually assembled. This procedure made it somewhat difficult to control the mass and mass distribution across the membrane surface to close tolerances. Despite the resulting small variations in device construction, the vibrational characteristics of the membrane and the modal correlation with performance were consistent and repeatable.

Membrane displacement data were collected at a discrete membrane point using MTI Instrument's Microtrak II (LTC-120-20) laser displacement sensor. The selected location for the discrete laser point was approximately one-quarter radius to the left of the membrane center, where it was least likely to be coincident with a membrane node. Auditory signals, which were used as one method of resonance detection, were picked up using a Sony ECM microphone. The input current and voltage were measured from the Trek model 609E-4 high voltage amplifier's built-in sensors. Pressure in the chamber and dynamic pressure at the nozzle exit were measured using two 5 in. H_2O D-4V pressure transducers from All Sensors Corporation. The dynamic pressure at the nozzle exit was transmitted to the pressure transducer using a pitot tube with a 1-mm-diam opening and overall length of tubing of 10 cm. The authors were aware that using a pitot tube for oscillating pressure measurements would result in lower detected dynamic pressures and velocities due to attenuation of the

[‡]Data available online at http://www.morpheus.umd.edu/research/active-flow-control/ejet.html [retrieved 10 April 2009].

[§]Data available online at http://music.nebrwesleyan.edu/wtt/index.html [retrieved 10 April 2009].

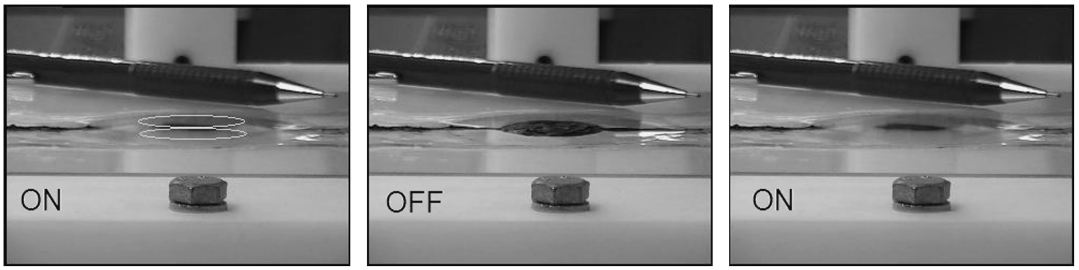

Fig. 4 Transverse vibration of membrane due to excitation at resonance (on–off–on sequence), with electrode border highlighted at the peak membrane displacements (±) in the leftmost image.

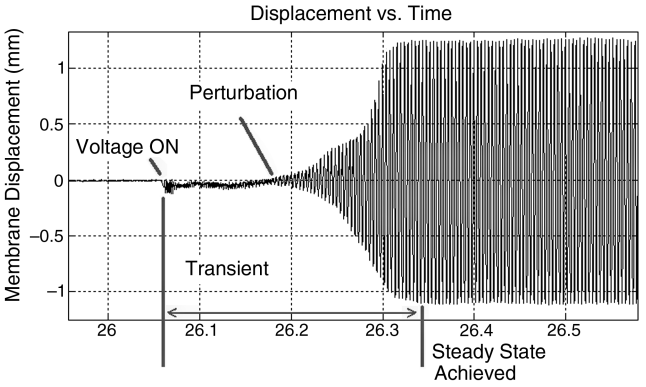

Fig. 5 The membrane response to periodic excitation [displacement (millimeters) vs time (s)].

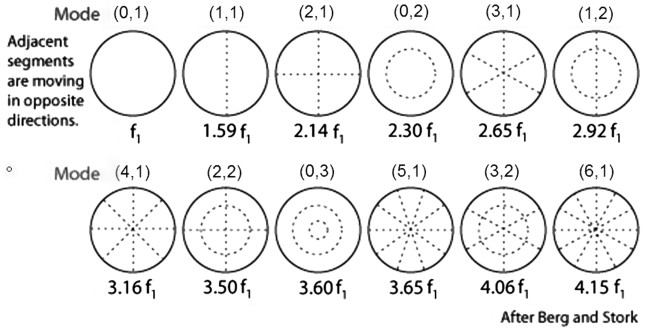

Fig. 6 Drum resonant modal series, displaying locations of circumferential and diametral node lines.

pressure signals in the tubing. Every precaution was taken to minimize the effects of pressure signal attenuation, including using the largest-diameter probe that was possible as well as keeping the tubing as short as possible [40]. Therefore, the velocities and pressures reported in this paper should be considered by the reader as minimum values, with the actual values being somewhat higher. Comparisons between induced velocities for each membrane mode, the main point of this paper, remain valid despite the presence of some pressure signal attenuation.

Data acquisition and experiment control were performed using a dSpace 1005 system. Data for each performance metric were sampled at 5 kHz. For the stroboscopic imaging, a Monarch Instruments stroboscope was used that was triggered by the excitation signal and was frequency-shifted to show a constant 1 Hz vibration at steady state. Video images of the stroboscopic tests were captured at 30 Hz using a digital camcorder. Scans of the membrane steady-state vibrations were performed using a PSV400 scanning laser vibrometer from Polytec.

IV. Parametric Device Study

During early device characterization, certain trends were determined [15]. Table 2 shows the device trends, including trends in transverse membrane displacement (displace), induced velocity at the nozzle exit (jet velocity), operating frequency at which best performance was observed (operating frequency), suppression of lower-frequency membrane mode shapes (low-frequency suppression), device power consumption, and the amount of time it takes the device to reach steady-state operation once the excitation is introduced (response).

The device behavioral trends that are listed across the top of Table 2 are related to decreasing values of device parameters listed down the left-hand side. Some parameter/trend combinations had no clear relationships and others had strong correlations. For instance, as the nozzle diameters or nozzle lengths were decreased, the induced velocity at the nozzle exit was increased, as would be expected. However, also as expected, this was a limited trend, in that as the nozzle length-to-diameter ratio approached a critical value, the viscous forces in the nozzle began to dominate, causing the induced velocity to drop off. Also, as the nozzle diameter is reduced, the suppression of low-frequency membrane modes is increasingly present, due to an increase in system impedance. It is this low-frequency suppression behavior that necessitates operation of the device at appropriate higher energy modes to achieve sufficiently high induced jet velocities.

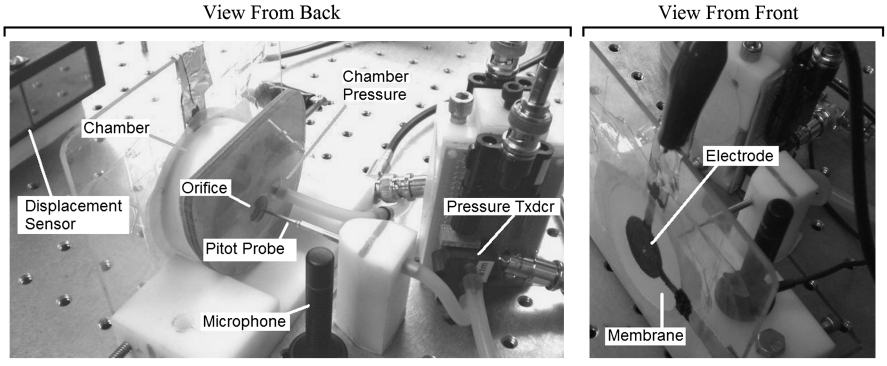

Fig. 7 E-jet characterization experiment layout: rear view (left) and front view (right).

Table 2 Observed E-jet device trends from parametric testing

Decreasing parameter	Metric trend[a]					
	Displace	Jet velocity	Operating frequency	Low-frequency suppression	Power consumption	Response
Nozzle diameter	|	↗	↓	↑	↑	|
Nozzle length	|	↗	↑	↓	↓	|
Electrode area (mass)	↓	↑	↑	|	↓	↓
Peak-to-peak voltage	↓	↓	|	|	↓	↓
Chamber height	|	|	↑	|	|	|

[a]The symbols ↑ denote increasing trend, ↗ denote limited trend, ↓ denote decreasing trend, and \| denote no clear trend.

Table 3 shows a subset of the experimental results from the parametric testing that was used to gain intuition about the system and to select a best-performing device geometry for subsequent testing. The table includes the variables chamber length L_c, nozzle diameter D_n, nozzle length L_n, electrode diameter D_e, maximum jet velocity at the nozzle exit $V_{\max}$, membrane vibration frequency at maximum velocity F_m, peak detected membrane displacement at maximum velocity $Z_{\max}$, peak-to-peak voltage amplitude V_{peak}, and rms power consumed at maximum velocity W_{rms}. All testing indicated in Table 3 employed a 50.8-mm-diam chamber and membrane. The membrane was biaxially prestrained 100 × 100%. In addition to the observed device trends described previously, the main conclusion the authors drew from the parametric testing is that this actuation scheme requires consistently small amounts of power over a wide range of device parameters.

In Table 3, the best-performing configuration is shown in bold for each test set, and the best-performing geometry selected from the configurations tested is shown in italics. The best-performing device geometry was selected based on lowest power consumption and highest induced-velocity performance from the preliminary parametric device characterization tests. It was this selected geometry that was used during subsequent modal testing. The selected device geometry was defined by a 5.1-cm-diam by 2.3-cm-long chamber, a 1.3-cm-diam by 0.5-cm-long cylindrical nozzle, and a 5.1-cm-diam by 0.03-mm-thick membrane.

Figure 8 shows typical data collected during a frequency sweep characterization for the selected E-jet device configuration. Both the presence of multiple resonances and the dramatically increased velocity performance, indicated by the high dynamic pressure at the nozzle, at one particular higher resonance are clear in the top graph, showing the fluctuating pressures inside the chamber and at the nozzle exit. Figure 8 also shows the identified resonant frequencies, with increasing label number associated with increasing excitation frequency at which the resonance was observed as well as the classical membrane mode shape associated with the numbered resonant frequency. The reader should note the low or nonexistent induced pressures for the membrane modes containing diametral nodes despite the large-amplitude vibrations: in particular, numbers 2, 3, 7, and 8. Because of nodal symmetry on the membrane, these modes induced a negligible volume change within the chamber. This would have been expected for the third membrane mode shapes as well (numbers 5, 6, 11, and 12) in an ideal system; however, these mode shapes were not perfectly symmetric, due to small asymmetries in the membrane construction. These asymmetries were chiefly caused by the radially asymmetric stiffness and mass distributions introduced by the electrode leads.

Frequency sweep characterizations were performed using a sinusoidal excitation at constant peak-to-peak voltage amplitude with linearly increasing excitation frequency. Resonant frequencies were identified by using pressure and displacement data when a chamber was included with the system and by using displacement and auditory signal data when the membrane was considered alone. Displacement data were inconclusive as an indicator of the relative magnitudes of modal displacements, because these were measured at a discrete point on the membrane and thus could potentially be in proximity to a node. Nevertheless, displacement data proved to be the most sensitive means of identifying system resonances. As mentioned previously, the location of the discrete displacement measurement was carefully chosen to avoid, as much as possible, the likelihood of being coincident with a membrane node.

Table 3 Selected experimental results from the E-jet parametric testing matrix

L_c, mm	D_n, mm	L_n, mm	D_e, mm	$V_{\max}$, m/s	F_m, Hz	$Z_{\max}$, mm	V_{peak}, V	W_{rms}, W
92.2	50.8	0.0	25.4	8.0	253	0.74	4000	0.67
92.2	12.7	25.4	25.4	9.8	196	1.41	4000	0.53
92.2	12.7	12.7	25.4	12.0	204	1.48	4000	0.40
92.2	12.7	5.3	25.4	11.5	210	1.41	4000	0.38
92.2	6.4	25.4	25.4	7.6	175	1.60	4000	0.63
92.2	**6.4**	**5.3**	**25.4**	**14.8**	**190**	**1.39**	**4000**	**0.42**
42.2	50.8	0.0	25.4	11.7	285	1.63	3500	0.96
42.2	12.7	25.4	25.4	11.6	223	1.18	3500	0.38
42.2	12.7	12.7	25.4	10.8	224	1.09	3500	0.50
42.2	12.7	5.3	25.4	12.5	230	1.40	3500	0.76
42.2	6.4	25.4	25.4	9.8	227	9.52	3500	0.68
42.2	6.4	12.7	25.4	9.2	229	1.28	3500	0.52
42.2	**6.4**	**5.3**	**25.4**	**15.0**	**234**	**1.41**	**3500**	**0.38**
22.5	50.8	0.0	25.4	10.9	284	0.99	3500	0.46
22.5	12.7	25.4	25.4	11.3	248	1.70	3500	0.33
22.5	12.7	12.7	25.4	12.9	255	1.25	3500	0.29
22.5	***12.7***	***5.3***	***25.4***	***14.8***	***263***	***1.15***	***3500***	***0.26***
22.5	6.4	25.4	25.4	8.8	238	1.54	3500	0.47
22.5	6.4	12.7	25.4	10.5	240	1.29	3500	0.40
22.5	6.4	5.3	25.4	13.5	245	1.40	3500	0.35
22.5	12.7	5.3	25.4	16.5	250	1.22	4000	0.79
22.5	12.7	5.3	25.4	14.4	250	0.82	3500	0.49
22.5	**12.7**	**5.3**	**12.7**	**17.5**	**282**	**1.16**	**4000**	**0.36**
22.5	12.7	5.3	12.7	14.8	282	0.72	3500	0.20

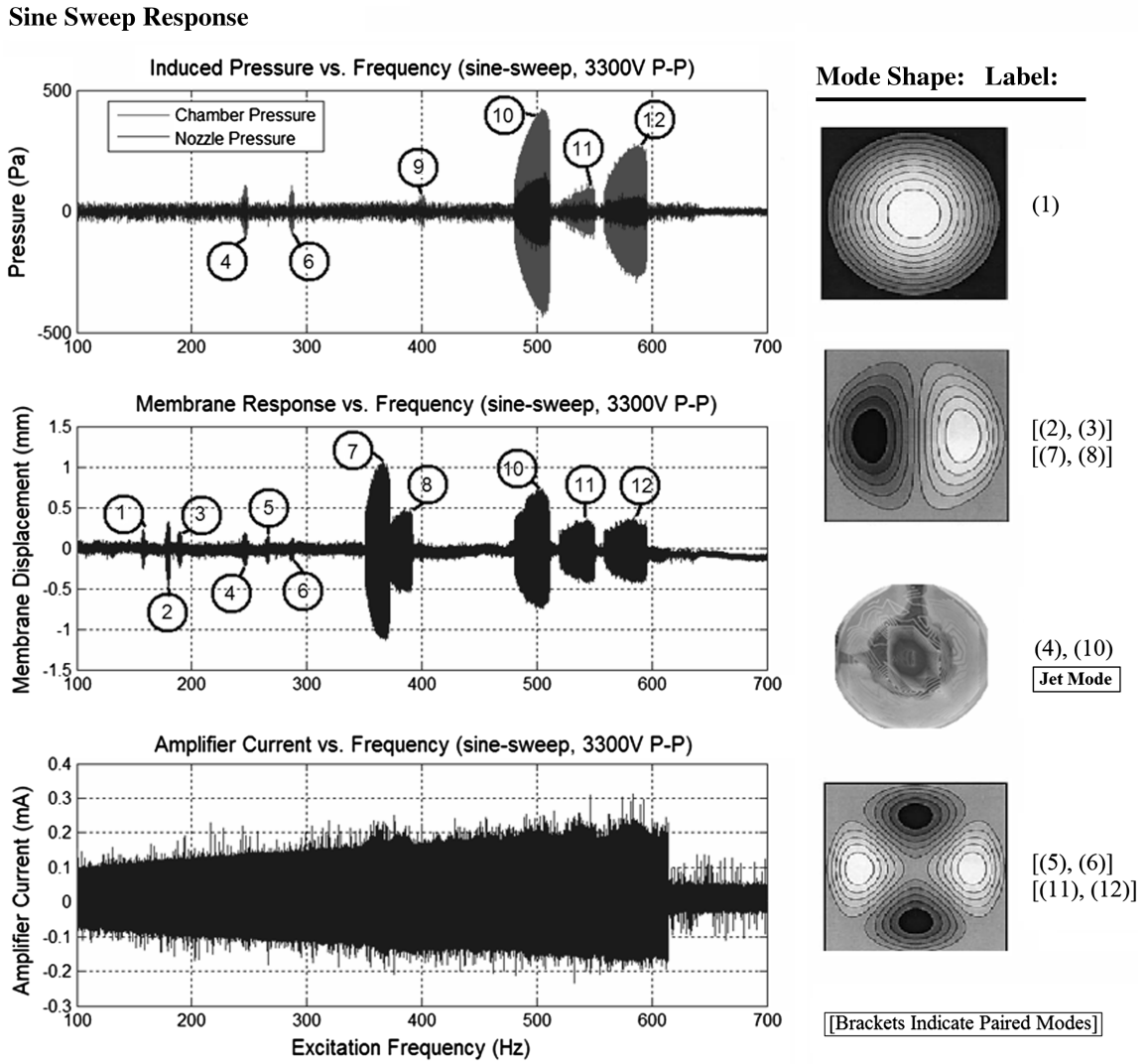

Fig. 8 A characteristic excitation frequency sweep response of an E-jet system. System resonances detected during scanning are indicated by circled numbers, and the associated membrane mode shape is indicated to the right. Orthogonally oriented paired modes are indictaed by bracketed numbers. Excitation was shut off at 620 Hz.

V. Stroboscopic Study

To qualitatively associate mode shape with device performance, a stroboscopic study was first performed. For this study, stroboscopic tests were performed at each resonant frequency detected during frequency sweep characterizations. For each stroboscopic test, the device was run at a single excitation frequency corresponding to one of the detected resonances for 5–10 s, during which time device performance metrics were recorded and the membrane dynamics were filmed. The stroboscope timing was slightly frequency-shifted from the membrane dynamics to slow down the dynamics enough to be detected by the video camera and the naked eye. It was quickly verified that membrane vibrational modes that included diametral nodes consistently yielded lower jet velocities than did modes with only circumferential nodes. Also verified were the presence of membrane modes that appeared to be classical in nature. Figure 9 shows the large displacements involved for the thin (0.03 mm) membrane as well as the significant variation in induced velocity for mode shapes approximating the second, third, and fourth classical membrane modes for one such stroboscopic test. Induced-velocity amplitude at the nozzle exit was 3, 4, and greater than 20 m/s for modes 2, 3, and what resembled mode 4, respectively. The first membrane mode is difficult to resolve in the photographic images, and so it is not included.

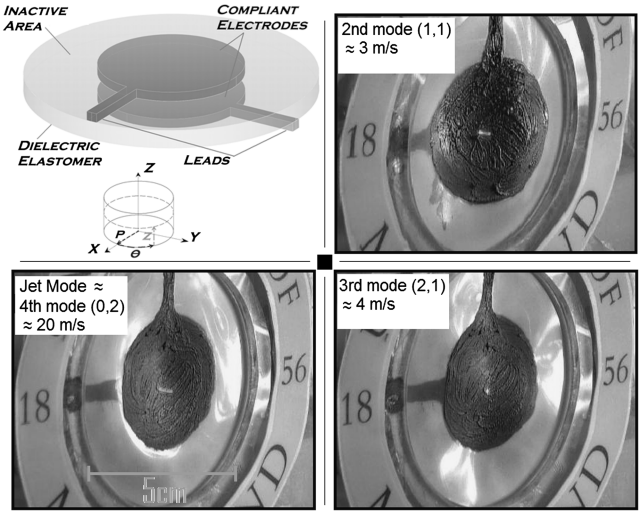

Fig. 9 Diaphragm diagram and still images taken from the stroboscopic study showing the second, third, and what appeared to be the fourth membrane mode shapes clockwise from top right.

VI. Laser Vibrometer Study

Once the stroboscopic study had verified both the presence of approximately classical modes and the association between diametral node lines and compromised velocity performance, a laser vibrometer study was designed to quantify the modes and corresponding velocity performance. Scanning laser vibrometer tests were performed to both identify and measure modal influence on device performance and to investigate the influence that device parameters such as electrode shape, electrode orientation, membrane prestrain, chamber size, and nozzle size had on the membrane dynamics. For purposes of brevity, only the results relating to the chamber and nozzle are discussed in this paper. Figure 10 shows the orientation of the scanning laser vibrometer with respect to the bench-mounted E-jet as well as the scanning grid used in each of the vibrometer tests.

These two images are included in this paper to affirm the assumption that any shift in point location on the membrane surface is negligible, due to the small angles and small (relative to the dimensions of the lab setup) transverse membrane displacements involved, which were on the order of millimeters. The scanning grid represents a total sweep in angle of approximately 3.7 deg across the membrane as measured from the laser origin. The distance between grid points is approximately 0.45 cm on the membrane, which represents a sweep angle of approximately 0.34 deg between grid points.

All vibrometer scans involved first performing a sine sweep characterization of the system to identify the detected resonant frequencies and then scanning the full membrane at each identified resonance. The results of the scans are presented as plots of membrane vibrational velocity isolines superimposed over an image of the membrane taken by the vibrometer during each test. Each scan is paired with the fast Fourier transform of the vibrometer data. The results of every scan relating to the content discussed in this paper are included in Appendix A.

The scans of the combined system (membrane, chamber, and nozzle) for the selected device geometry in Figs. A1–A12 represent the vibrometer scanning data for each of the resonances indicated in Fig. 8 and are displayed in ascending order of excitation frequency supplied as a dc-offset sinusoid at 3300 V peak to peak.

The vibrometer scans for the membrane alone without a chamber or nozzle attached are shown in Figs. A13–A18. The membrane was different from that used for the combined system scans indicated in Figs. A1–A12.

The vibrometer scans for the membrane with the chamber and nozzle subsystems attached are shown in Figs. A19–A24. The same membrane was used as for membrane-alone scans indicated in Figs. A13–A18. These figures result from an excitation of 3600 V peak to peak.

The vibrometer scans for the membrane with a fully enclosed chamber subsystem attached (i.e., sealed-off nozzle subsystem) are shown in Figs. A25–A31. The same membrane was used as in the scans indicated in Figs. A13–A18 and Figs. A19–A24.

Each full vibrometer scan lasted 50 s, because the dwell time at each of the 100 grid points was set to be $\frac{1}{2}$ s. For the large majority of resonant frequencies identified, the membrane exhibited clean steady-state vibrations that yielded clean vibrometer scans. There were occasionally, however, resonant frequencies at which the vibrations were not entirely steady throughout the entire scan time, making the vibrometer scan difficult to perform, although not impossible. One such scan is shown in Fig. A9 in Appendix A. The authors were also able to observe the unsteady vibrations with the naked eye using the stroboscope.

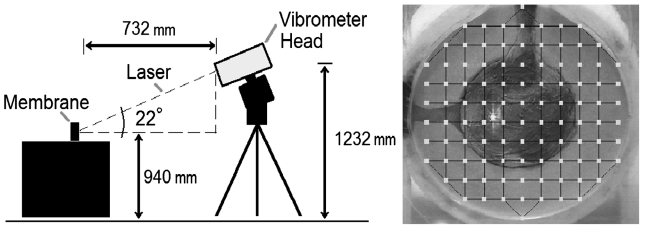

Fig. 10 Laser vibrometer laboratory setup (left image), and 100-point scanning grid projected onto a photo of the 5-cm-diam membrane (right image). The electrode shown is 2.5 cm in diameter.

Two complete sets of vibrometer tests, out of a total of 13 sets, are discussed in this section. The first set of tests (indicated in Figs. A1–A12) was performed to gain a better understanding of the contribution and nature of the most significant membrane mode that consistently yielded the best velocity performance, hereafter referred to as the *jet mode*. This first set of vibrometer tests relates directly to the data presented in Fig. 8, which were used to identify each of the resonant excitation frequencies at which to scan. The results from the scans in the first set of tests, referred to as the jet-mode tests, are included in their entirety in Appendix A. For this set of tests, the evaluated system included the membrane, the chamber, and the nozzle subsystems. The resulting vibrometer scans revealed that the membrane subsystem exhibits paired modes as well as a repeated modal series. An example of two paired modes can be seen in Figs. A2 and A3. Note that the paired modes are close together in frequency, but are orthogonal to one another in shape. The repeated modal series occurred as the excitation frequency was increased. For each integer multiple of the fundamental modal frequency, the excitation frequency excited that mode. For instance, the fundamental modal frequency for the second mode was 177.5 Hz, as shown in Fig. A2. As the excitation frequency was increased to approximately twice the fundamental frequency of the second mode, that mode reappears in the system, but at a higher energy level, as shown in Fig. A7. This trend of repeating series was later verified for the third and fourth excitation frequency multiples of the membrane resonant frequencies.

When the excitation frequency is matched to the vibrational frequency, the membrane is being forced to return to the plane once per cycle when the voltage drops off and the membrane is returned to its nominal condition of maximum effective stiffness. Likewise, when the excitation frequency is twice the vibrational frequency, the membrane is being forced twice per cycle and so attains greater vibrational amplitude due to the higher energy input into the system. All detected modes were observed repeating in the experiments, except for the first membrane mode, which was not observed to repeat.

The experimentally observed presence of paired modes, the observed repeated modal series, and the method of exciting these higher-order modes by periodically varying membrane stiffness represent a new contribution to experimental membrane dynamic studies. Because only a small number of experimental membrane studies [22] are currently available in the literature, these results thus represent an important contribution to the experimental study of membrane dynamics and can be used to inform future membrane modeling efforts.

Although these are intriguing new results, the principal objective of the jet-mode tests was to identify, quantify, and describe the jet mode as it relates to E-jet device performance. The jet mode is shown in both Fig. A4, representing a once-per-cycle forcing, and in Fig. A10, with a twice-per-cycle forcing. Because of excitation at twice the vibrational frequency of the mode shown in Fig. A10, it exhibited a much greater induced velocity of ± 16 m/s at the nozzle exit, as opposed to ± 7 m/s for the same mode shape in Fig. A4. Again, this was due to a higher energy input to the membrane at the higher excitation frequency. Although the mode appears in the stroboscopic study images such as the classical fourth membrane mode, the vibrometer scans reveal that it is not. Notably, the jet mode appears third in order of increasing vibrational frequency, rather than fourth, as would be expected in the classical case. Although the jet-mode shape does contain a full circumferential node, its location is closer to the center than would be expected, and the outer vibrational ring is not complete, appearing almost as a (1,1) mode shape for an annular membrane [41]. It appears from this set of vibrometer scans that the jet mode is some type of degenerate mode. More analysis must be performed to fully characterize and understand the jet mode. The authors conclude from this set of tests that one higher-order vibrational

mode (the jet mode) is to be exploited for best device performance and that best results are obtained when the excitation frequency is twice the vibrational frequency of the jet mode.

The second set of vibrometer tests discussed in this paper was performed to isolate coupling effects between the membrane, chamber, and nozzle subsystems. The results of these tests are also included in Appendix A. A new membrane was assembled and used for all of the coupling tests. For the first portion of the coupling tests, the membrane subsystem was examined alone without any chamber or nozzle attached. These results are shown in Figs. A13–A18. The same procedure was followed, first performing a sine sweep to identify the resonant frequencies. Auditory signal replaced chamber pressure as the second set of data used to identify resonances in addition to membrane displacement. What is interesting to note from these tests is that for the membrane subsystem alone, the jet mode does not appear. From this result, the authors inferred that the jet mode is coupled to either the chamber subsystem, the nozzle subsystem, or to both.

The second portion of the coupling tests involved testing the membrane in combination with both the chamber and the nozzle subsystems. The results are shown in Figs. A19–A24. The jet mode once again appears in this set of coupling tests.

In the final portion of the coupling tests, the nozzle was sealed off so that only the membrane and chamber subsystems were included. The results for these tests are shown in Figs. A25–A31. The jet mode appears once again. Note the increased amplitude seen in Fig. A29 without the nozzle when compared with Fig. A22 with the nozzle, which implies that the predominant coupling effect is due to the chamber. Also, note the reduction in frequency associated with the sealed off nozzle. This is consistent with a system coupled to the chamber, because the acoustical resonant frequency of the chamber is reduced as the nozzle diameter is reduced, attaining a minimum value when the nozzle diameter is zero.

VII. Conclusions

The influence of membrane structural dynamics on membrane-driven synthetic jet performance for a new synthetic jet actuation method employing electrically excited acrylic dielectric elastomer membranes was investigated. Classical membrane mode shapes have been identified as the predominant characteristic of the dynamic membrane subsystem, which is used as the jet actuator in the E-jet device. Overall device performance has been determined to be highly dependent on which mode is excited on the membrane. One particular higher-order mode, the jet mode approximating the appearance of the fourth classical membrane mode and exhibiting degenerate characteristics, gives dramatically better induced-velocity performance at the nozzle than any other membrane mode. Furthermore, the jet mode yields the best device performance when it is excited at twice its vibrational frequency. The jet mode exhibits clear coupling with the chamber subsystem, because it does not appear when the chamber subsystem is not included. Further work is needed to more fully understand, characterize, and model the fluid–structure coupling behavior exhibited by the device and the resulting correlation with overall synthetic jet velocity performance.

This paper has presented a new means of generating a synthetic jet using a thin, low-modulus, acrylic dielectric elastomer. This new method of actuation represents an attractive, mechanically simple, lightweight, and efficient low-power alternative to piezoceramic and electromagnetically driven synthetic jet designs. The experimental membrane dynamics results presented in this paper represent a new contribution to the experimental study of membrane dynamics and will be used by the authors to inform future membrane and device modeling efforts. This paper has also presented the first documented case in which the application of higher-order membrane vibrational modes is clearly associated with significant increases in synthetic jet performance. The authors believe that the methodology of exploiting higher-order modes to gain increases in membrane-driven synthetic jet performance may be applicable to other synthetic jet designs and, as such, may represent a new operating paradigm for similar classes of systems with low-mechanical-impedance driving mechanisms.

Because of the low frequency of operation and good induced nozzle velocity performance of greater than 25 m/s, the E-jet seems to be well suited to low-speed active flow control applications. Planned directions for future work include developing an experimentally validated geometrically and materially nonlinear finite element model for the coupled fluid–structure system to more fully explore the device design space, deriving a lumped-parameter model approximation of the system, optimizing the device design using impedance matching techniques, testing a better electrode material less prone to arcing during operation, developing a more automated device assembly process, and implementation and testing of an E-jet array on a test article. The authors expect to encounter a significant impact to future lumped-parameter modeling efforts, due to the change in the traditional assumption of a piston or first membrane mode shape to the higher-order coupled jet mode.

Appendix A: Vibrometer Scans

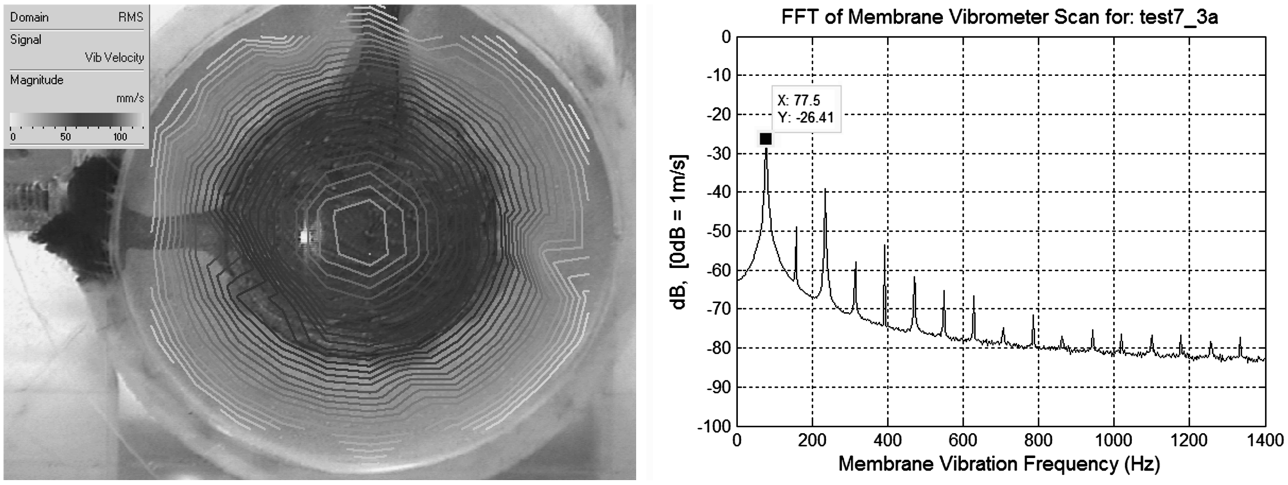

Fig. A1 Vibrometer scan at the first detected resonant frequency at 157 Hz excitation and 78 Hz vibration with a maximum rms vibrational velocity of 0.113 m/s at the center. Induced nozzle velocity is negligible.

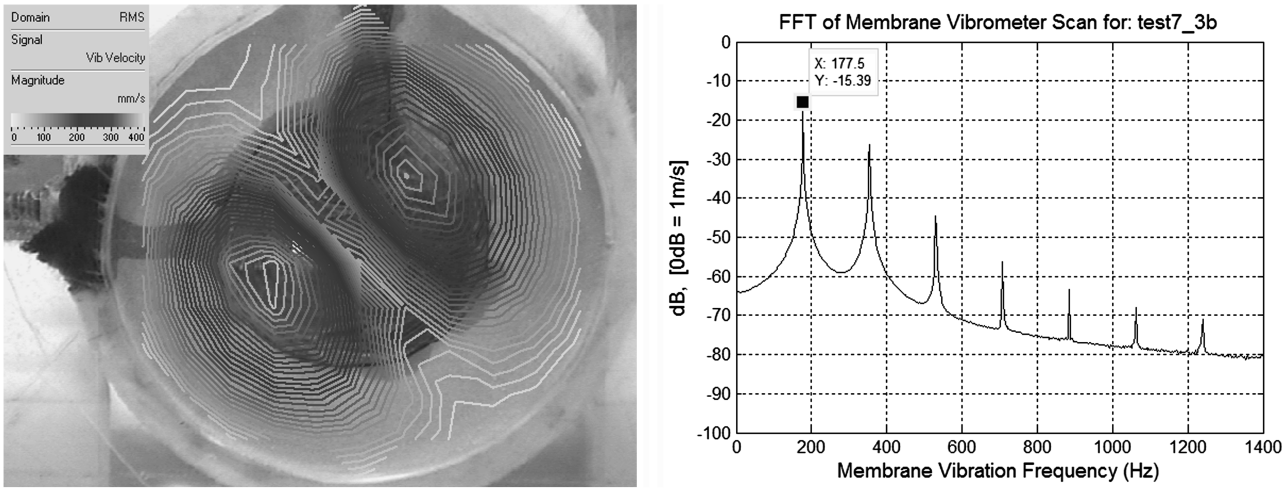

Fig. A2 Vibrometer scan at the second detected resonant frequency at 177 Hz excitation and 177.5 Hz vibration with a maximum rms vibrational velocity of 0.397 m/s at two points. Induced nozzle velocity is negligible.

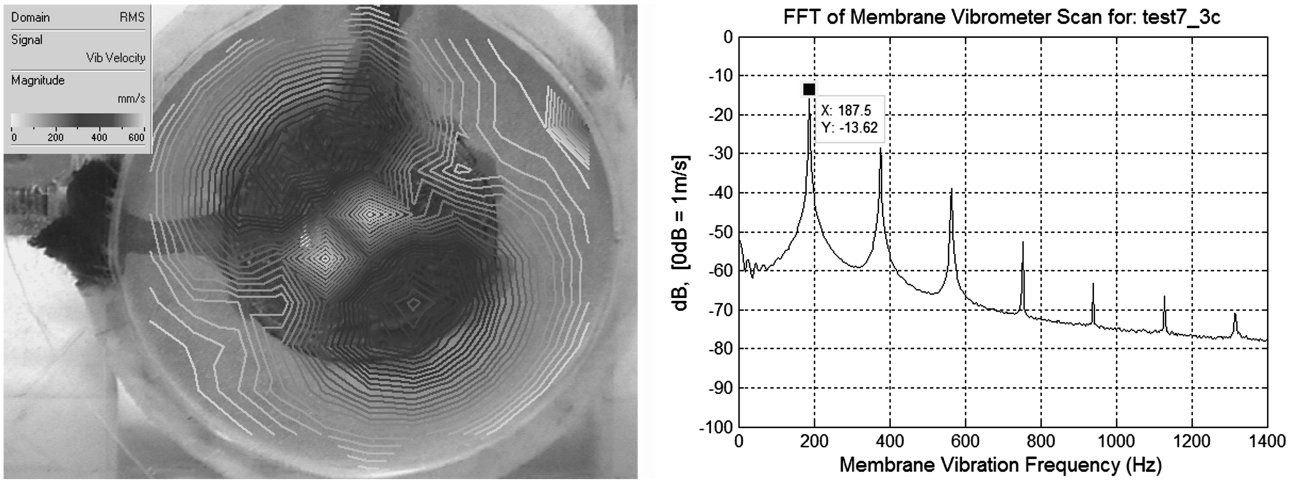

Fig. A3 Vibrometer scan at the third detected resonant frequency at 188 Hz excitation and 187.5 Hz vibration with a maximum rms vibrational velocity of 0.503 m/s at two points. Induced nozzle velocity is ±2 m/s.

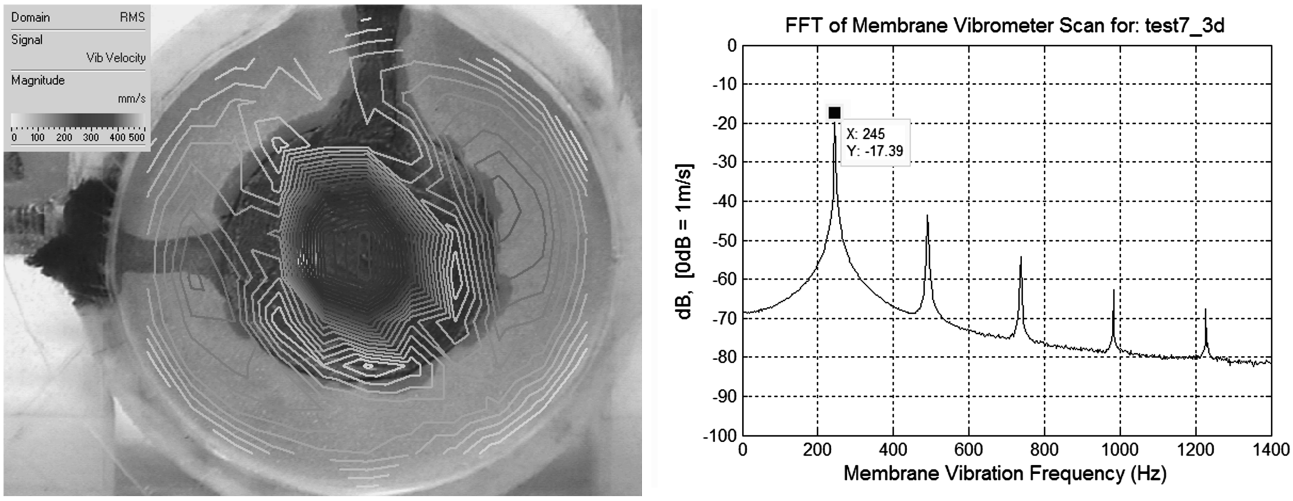

Fig. A4 Vibrometer scan at the fourth detected resonant frequency at 245.5 Hz excitation and 245 Hz vibration with a maximum rms vibrational velocity of 0.403 m/s at a single point in the center. Induced nozzle velocity is ±7 m/s.

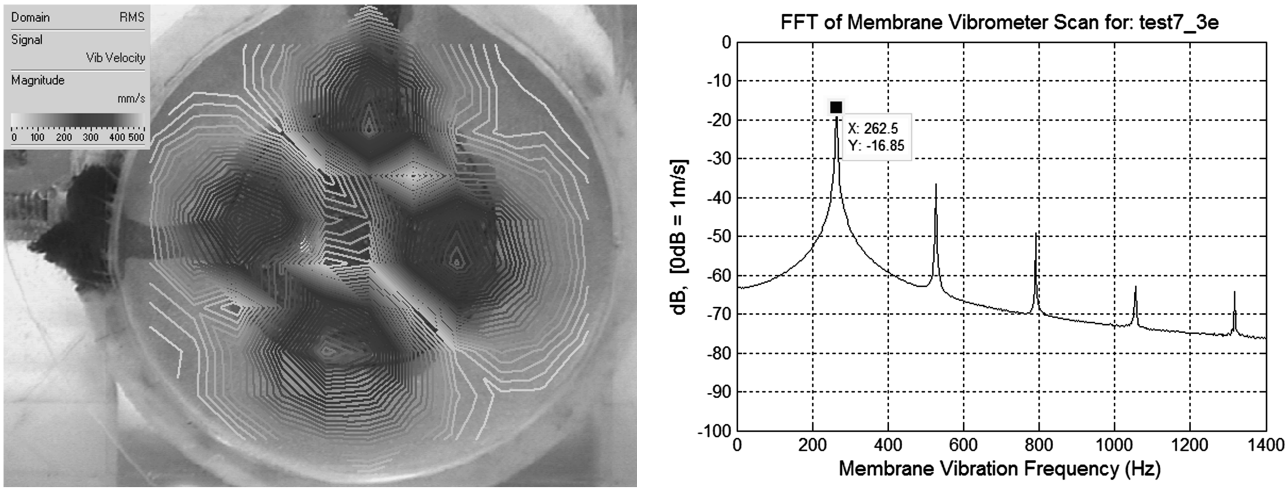

Fig. A5 Vibrometer scan at the fifth detected resonant frequency at 263.5 Hz excitation and 262.5 Hz vibration with a maximum rms vibrational velocity of 0.453 m/s at four points. Induced nozzle velocity is ±5 m/s.

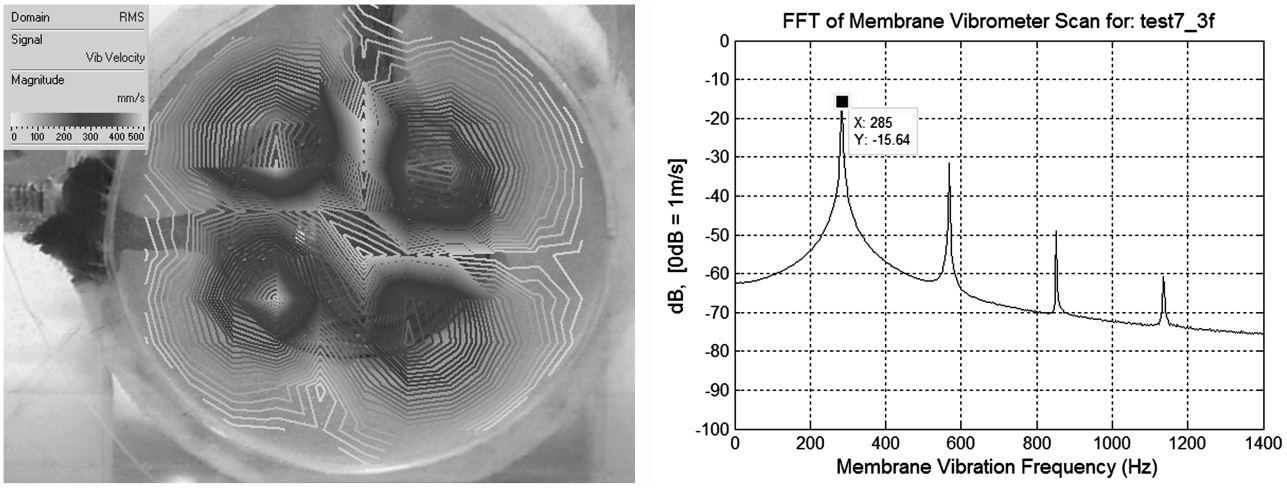

Fig. A6 Vibrometer scan at the sixth detected resonant frequency at 284 Hz excitation and 285 Hz vibration with a maximum rms vibrational velocity of 0.499 m/s at four points. Induced nozzle velocity is ±4 m/s.

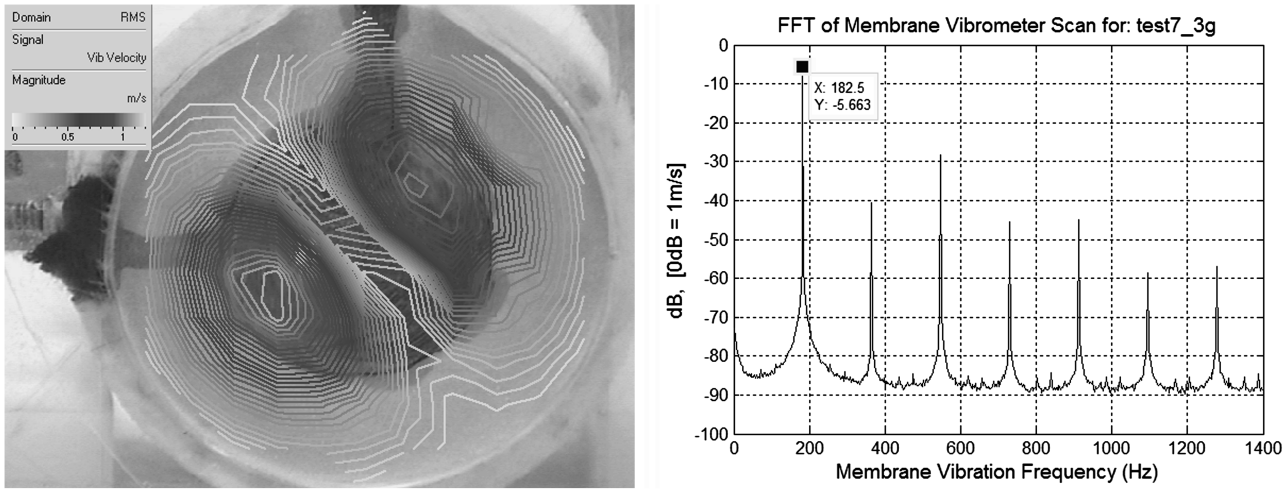

Fig. A7 Vibrometer scan at the seventh detected resonant frequency at 365 Hz excitation and 182.5 Hz vibration with a maximum rms vibrational velocity of 1.16 m/s at two points. Induced nozzle velocity is ±5 m/s.

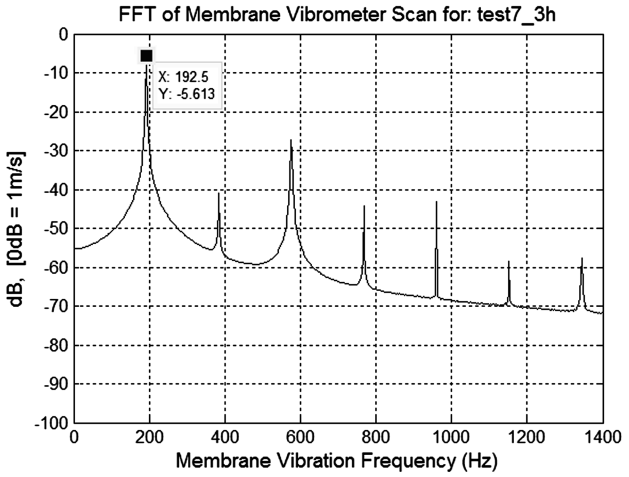

Fig. A8 Vibrometer scan at the eighth detected resonant frequency at 384 Hz excitation and 192.5 Hz vibration with a maximum rms vibrational velocity of 1.24 m/s at two points. Induced nozzle velocity is negligible.

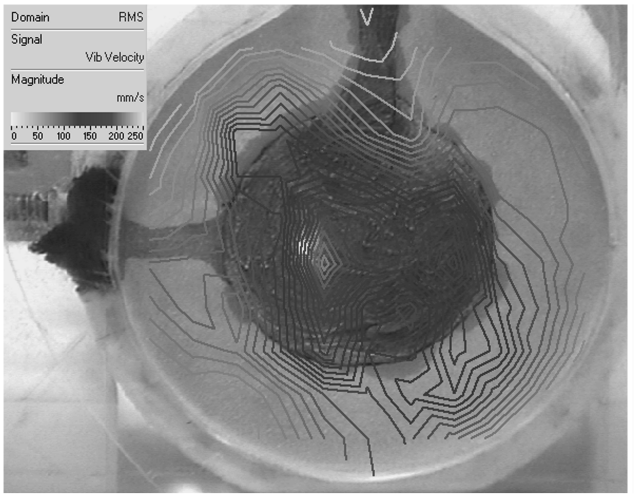

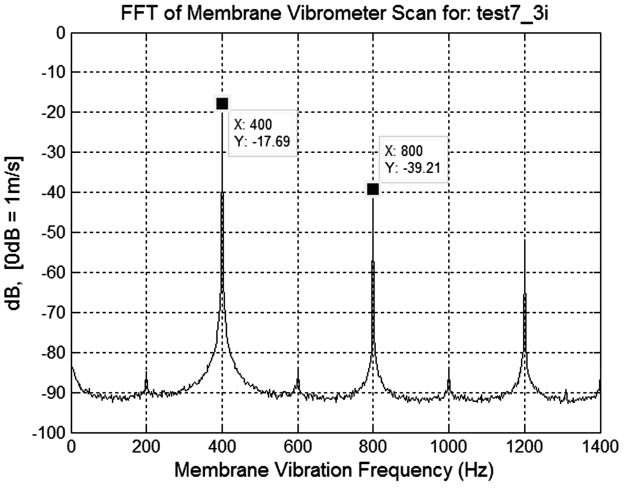

Fig. A9 Vibrometer scan at the ninth detected resonant frequency at 400 Hz excitation and 400 Hz vibration with a maximum rms vibrational velocity of 0.299 m/s near the center. Induced nozzle velocity is ±4 m/s.

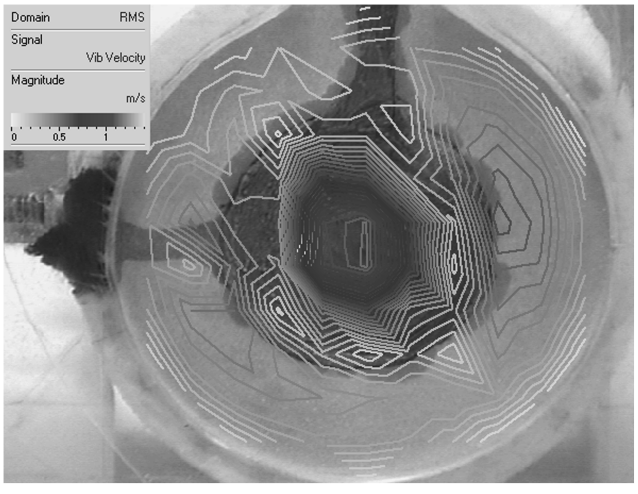

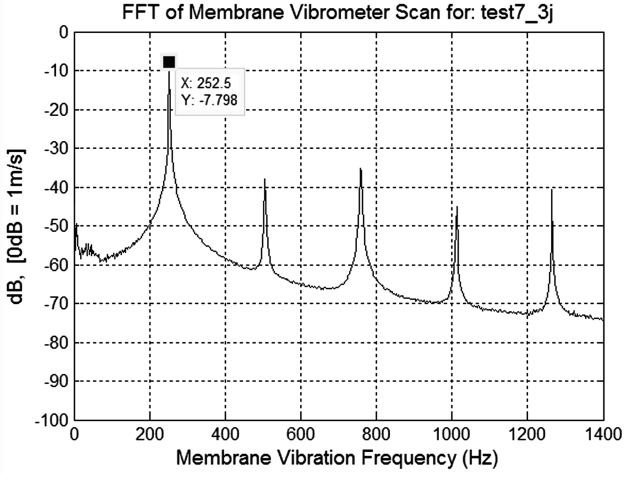

Fig. A10 Vibrometer scan at the 10th detected resonant frequency at 505.8 Hz excitation and 252.5 Hz vibration with a maximum rms vibrational velocity of 1.21 m/s at the center. Induced nozzle velocity is ±16 m/s (peak velocity for this test series).

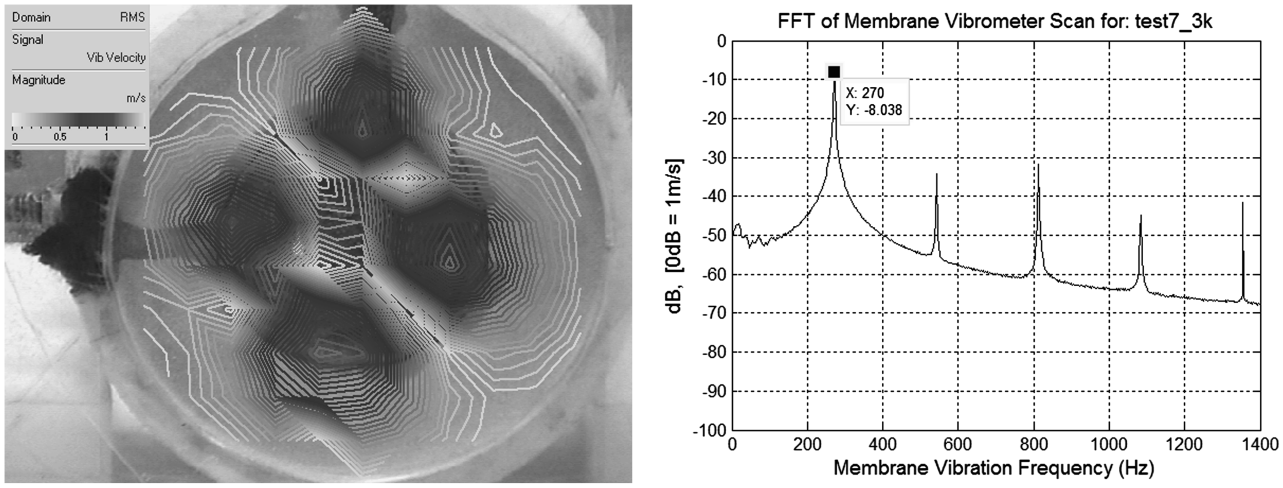

Fig. A11 Vibrometer scan at the 11th detected resonant frequency at 542 Hz excitation and 270 Hz vibration with a maximum rms vibrational velocity of 1.22 m/s at four points. Induced nozzle velocity is ±7.5 m/s.

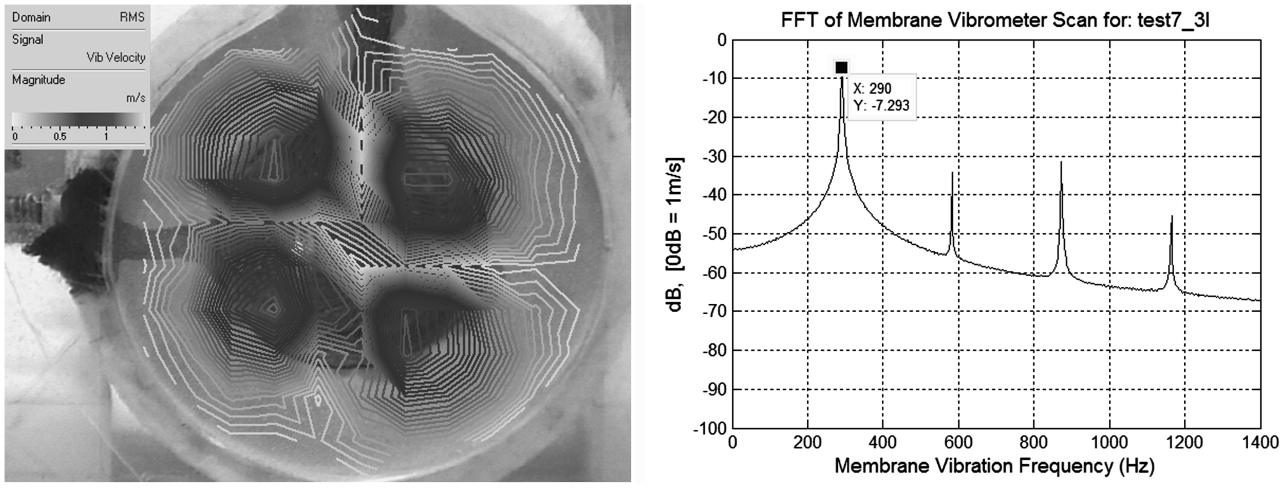

Fig. A12 Vibrometer scan at the 12th detected resonant frequency at 582 Hz excitation and 290 Hz vibration with a maximum rms vibrational velocity of 1.23 m/s at four points. Induced nozzle velocity is ±6 m/s.

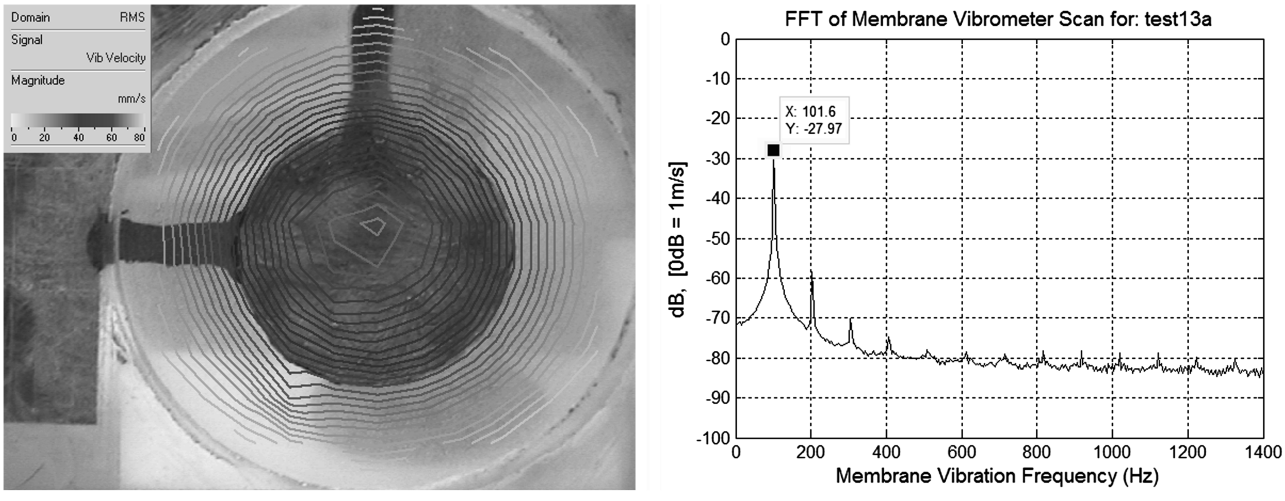

Fig. A13 Vibrometer scan at the first detected resonant frequency at 102 Hz excitation and 101.6 Hz vibration with a maximum rms vibrational velocity of 0.071 m/s at the center.

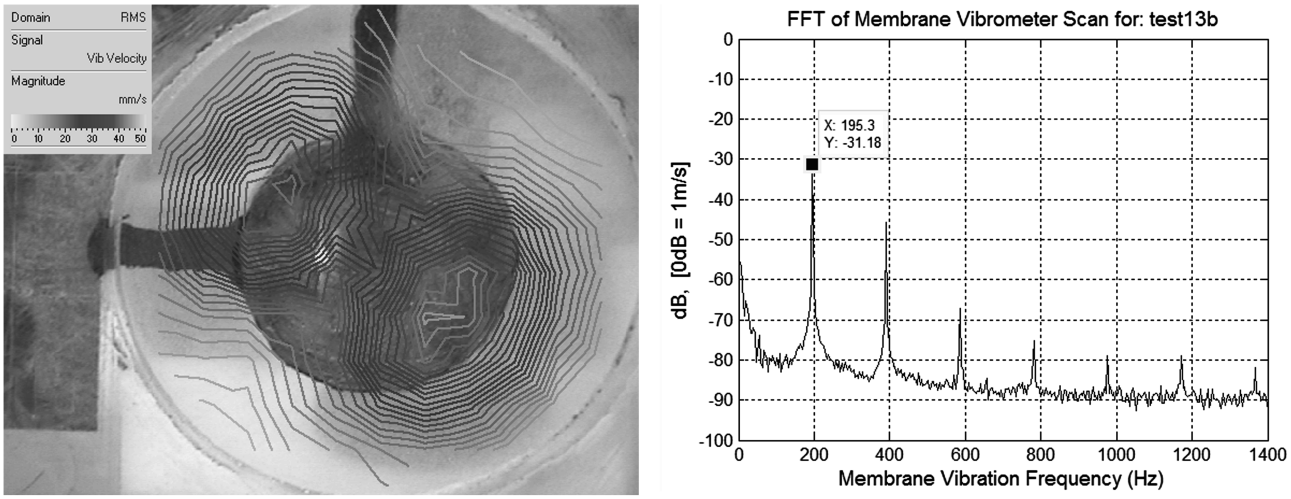

Fig. A14 Vibrometer scan at the second detected resonant frequency at 195.2 Hz excitation and 195.3 Hz vibration with a maximum rms vibrational velocity of 0.055 m/s at two points.

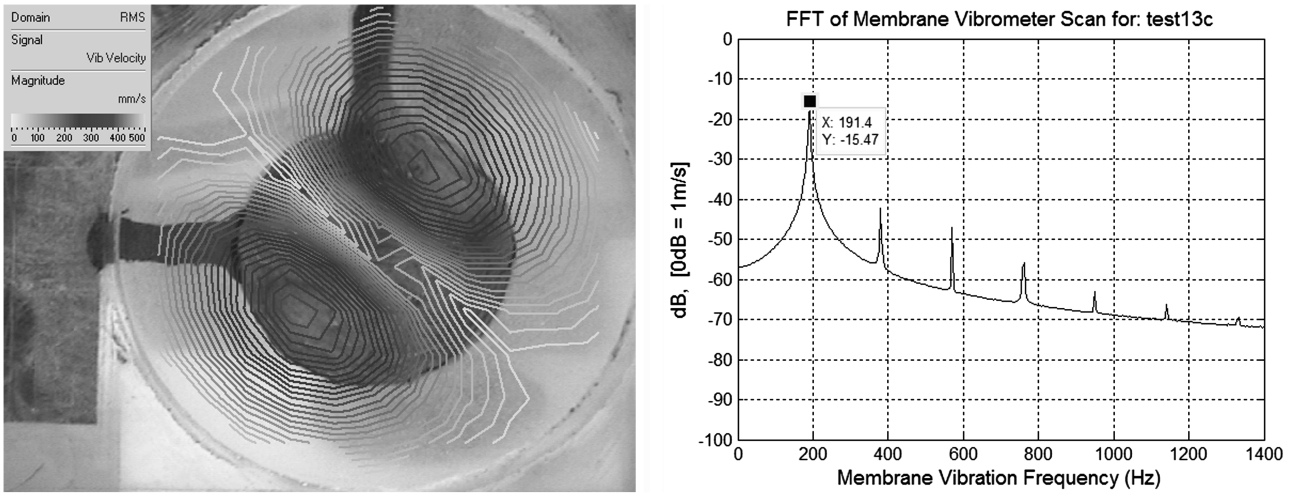

Fig. A15 Vibrometer scan at the third detected resonant frequency at 380 Hz excitation and 191.4 Hz vibration with a maximum rms vibrational velocity of 0.412 m/s at two points.

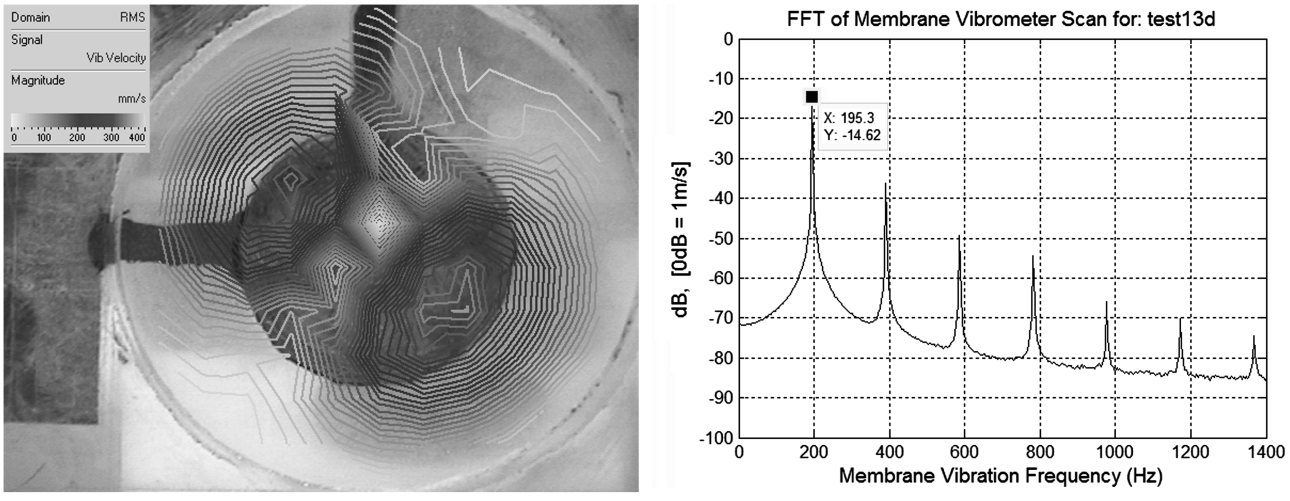

Fig. A16 Vibrometer scan at the fourth detected resonant frequency at 391 Hz excitation and 195.3 Hz vibration with a maximum rms vibrational velocity of 0.368 m/s at two points.

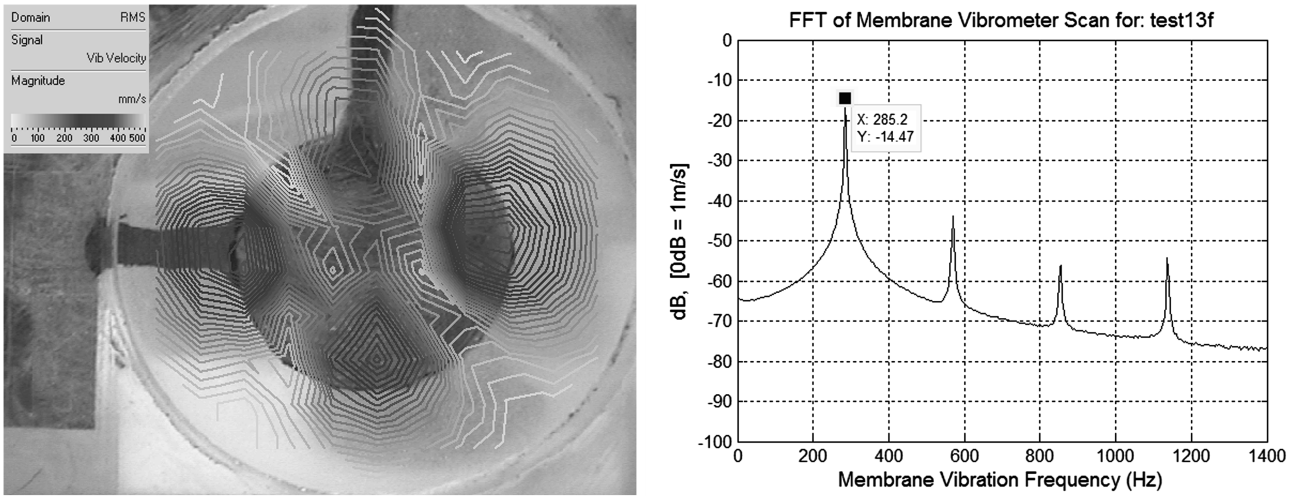

Fig. A17 Vibrometer scan at the fifth detected resonant frequency at 569 Hz excitation and 285.2 Hz vibration with a maximum rms vibrational velocity of 0.403 m/s at four points.

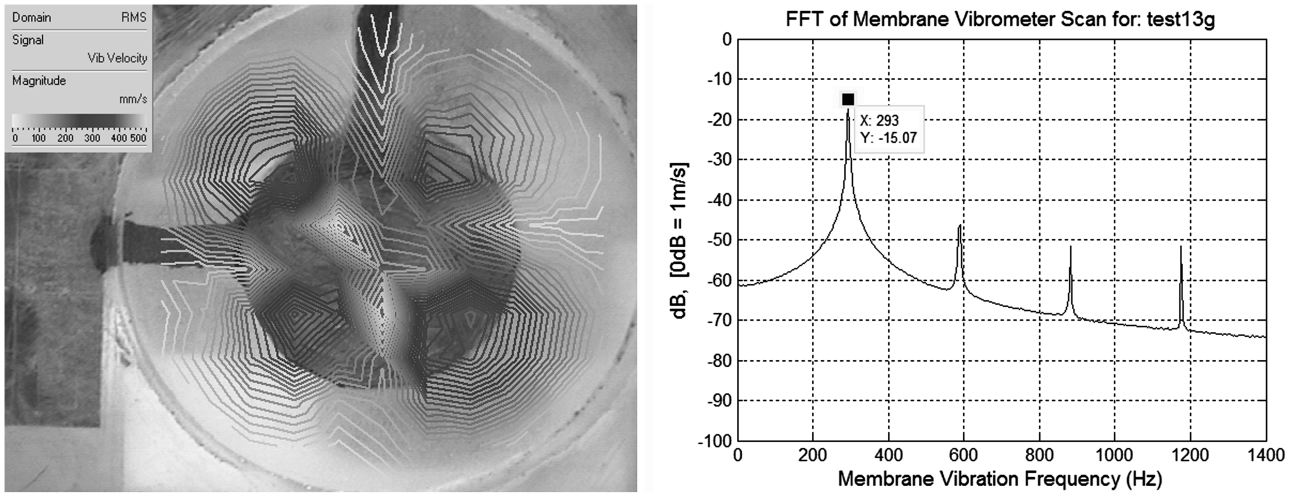

Fig. A18 Vibrometer scan at the sixth detected resonant frequency at 588 Hz excitation and 293 Hz vibration with a maximum rms vibrational velocity of 0.422 m/s at four points.

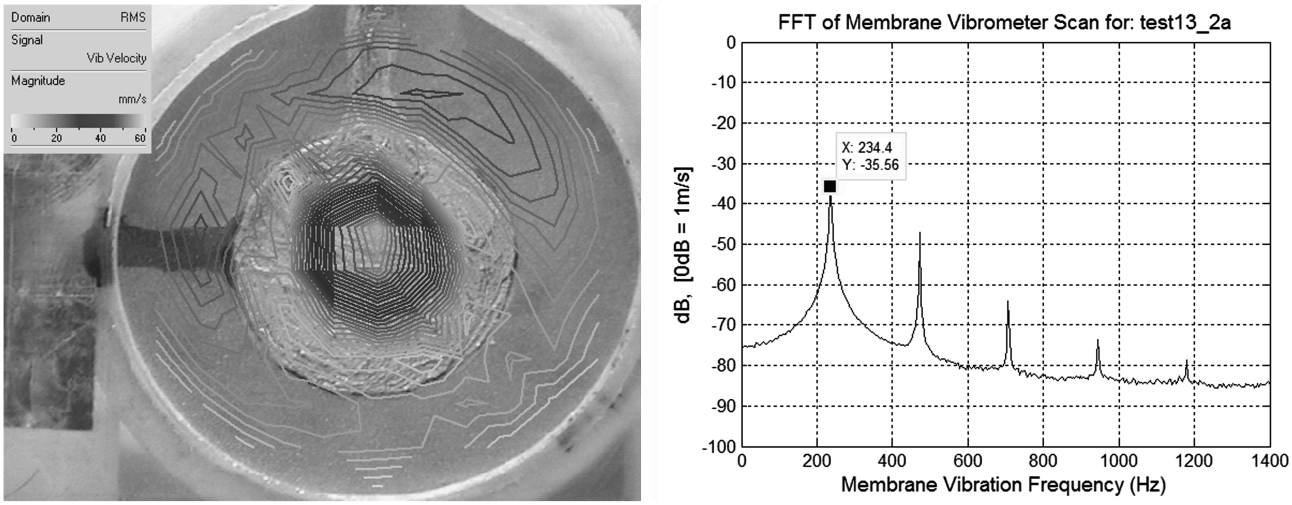

Fig. A19 Vibrometer scan at the first detected resonant frequency at 236 Hz excitation and 234.4 Hz vibration with a maximum rms vibrational velocity of 0.057 m/s at the center.

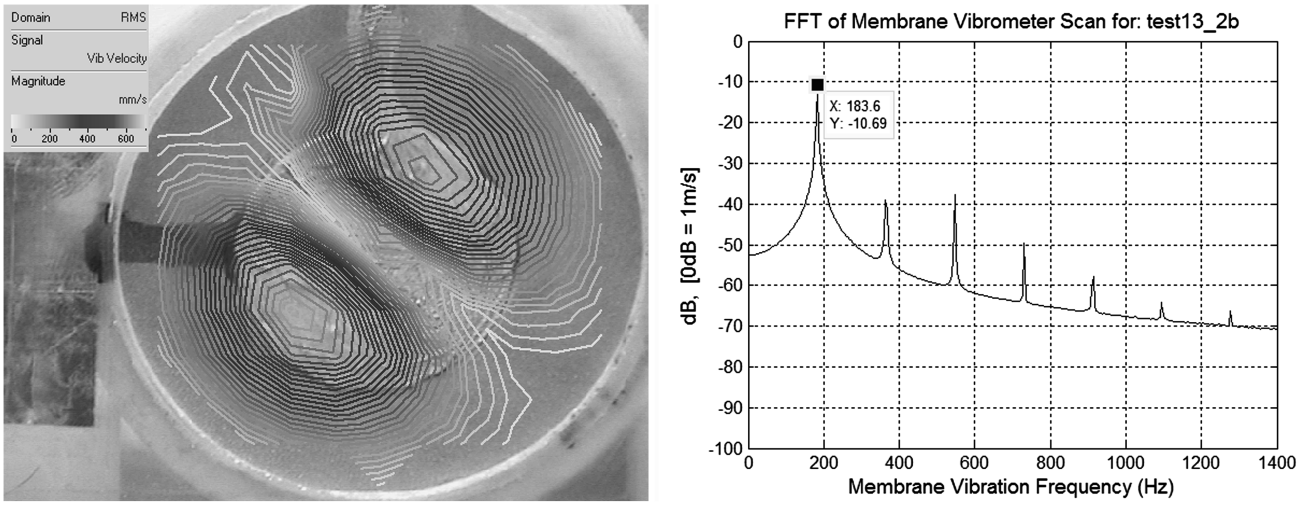

Fig. A20 Vibrometer scan at the second detected resonant frequency at 365 Hz excitation and 183.6 Hz vibration with a maximum rms vibrational velocity of 0.677 m/s at two points.

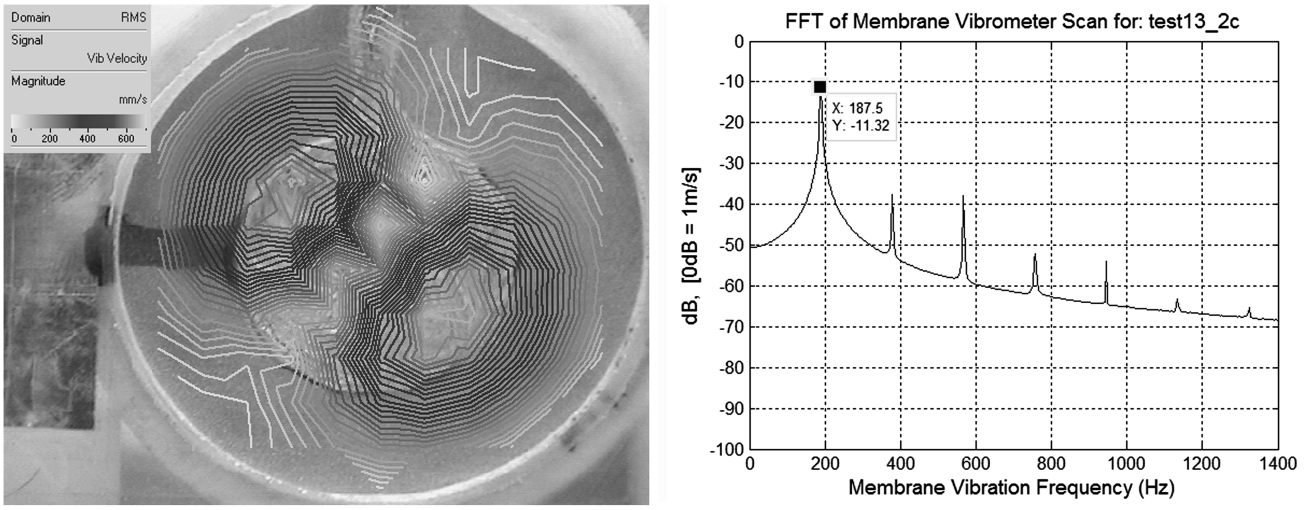

Fig. A21 Vibrometer scan at the third detected resonant frequency at 378 Hz excitation and 187.5 Hz vibration with a maximum rms vibrational velocity of 0.682 m/s at two points.

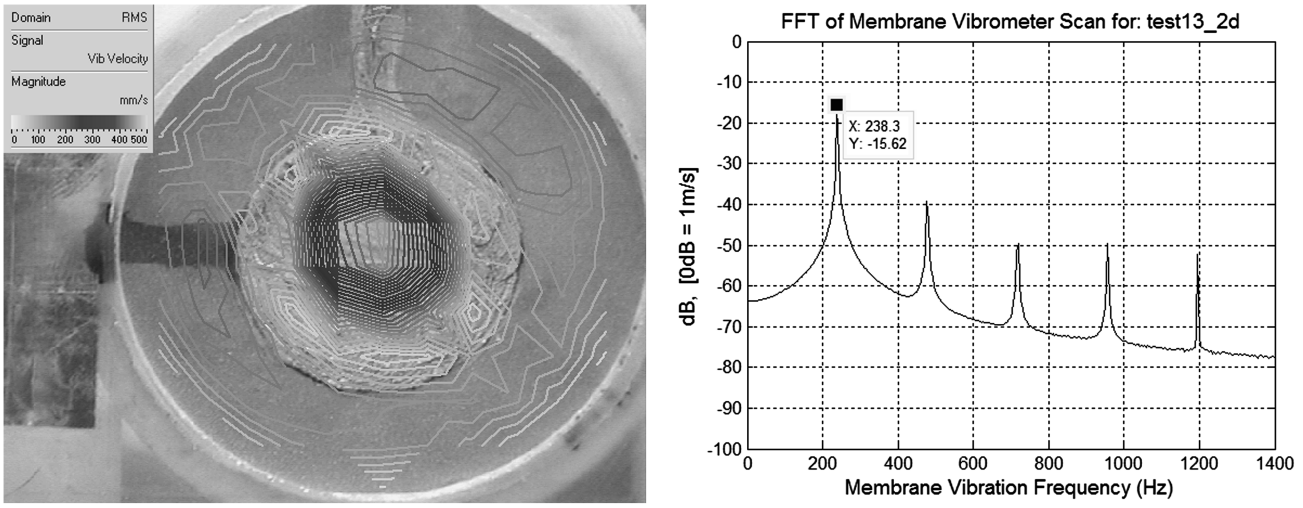

Fig. A22 Vibrometer scan at the fourth detected resonant frequency at 478 Hz excitation and 238.3 Hz vibration with a maximum rms vibrational velocity of 0.467 m/s at the center.

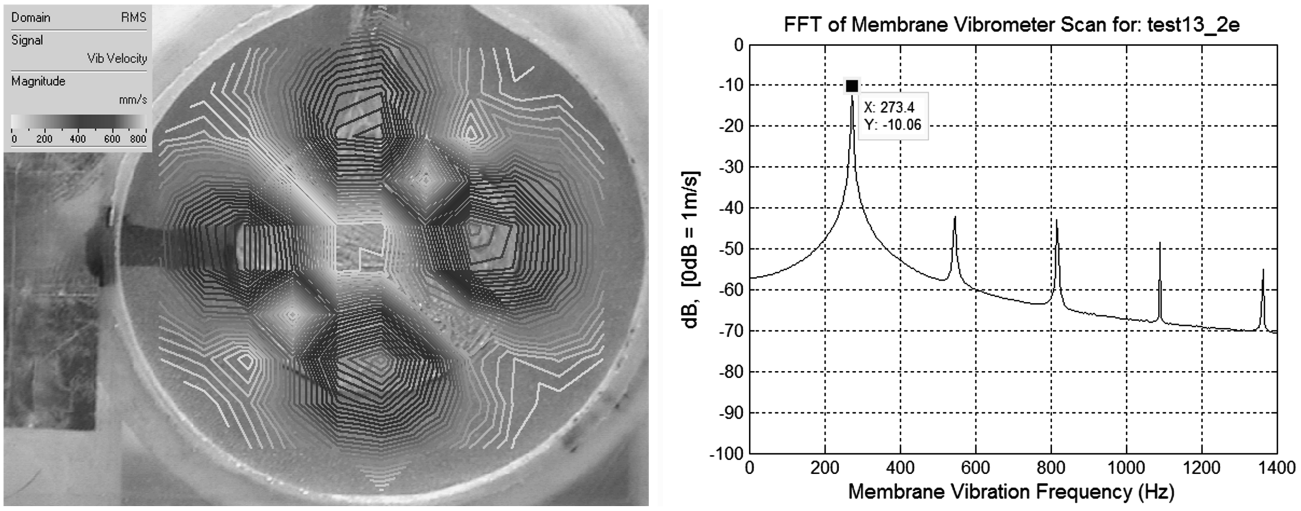

Fig. A23 Vibrometer scan at the fifth detected resonant frequency at 545 Hz excitation and 273.4 Hz vibration with a maximum rms vibrational velocity of 0.726 m/s at four points.

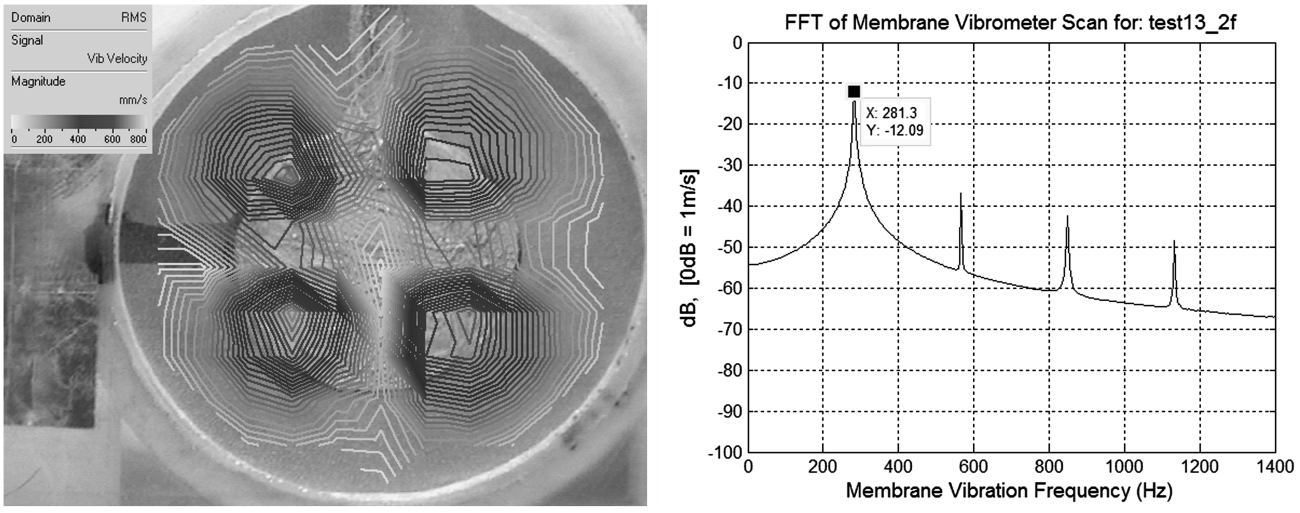

Fig. A24 Vibrometer scan at the sixth detected resonant frequency at 566 Hz excitation and 281.3 Hz vibration with a maximum rms vibrational velocity of 0.731 m/s at four points.

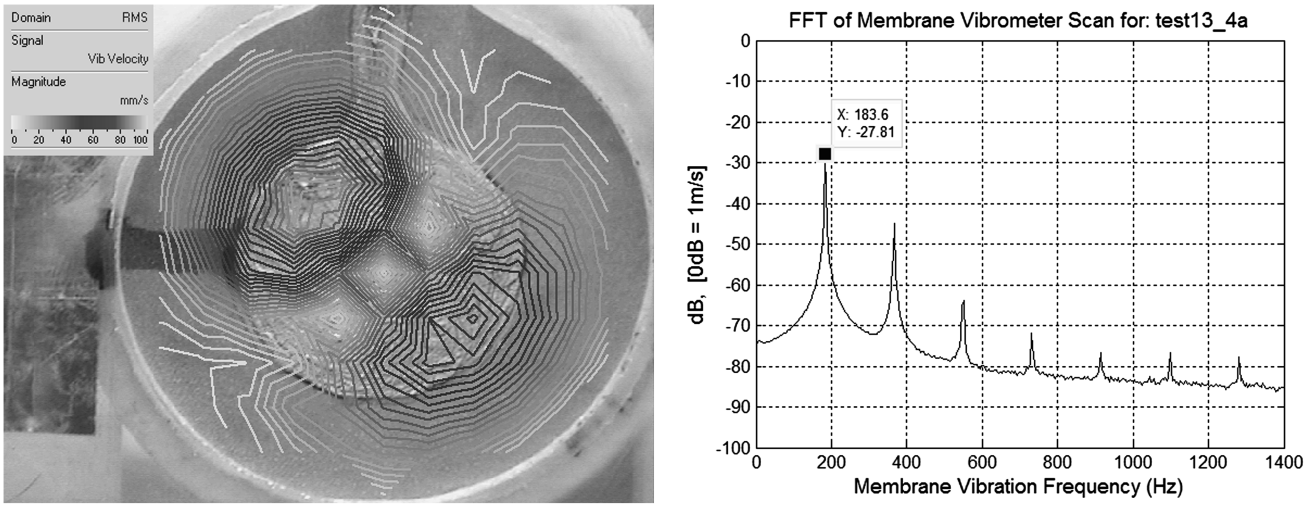

Fig. A25 Vibrometer scan at the first detected resonant frequency at 183 Hz excitation and 183.6 Hz vibration with a maximum rms vibrational velocity of 0.094 m/s.

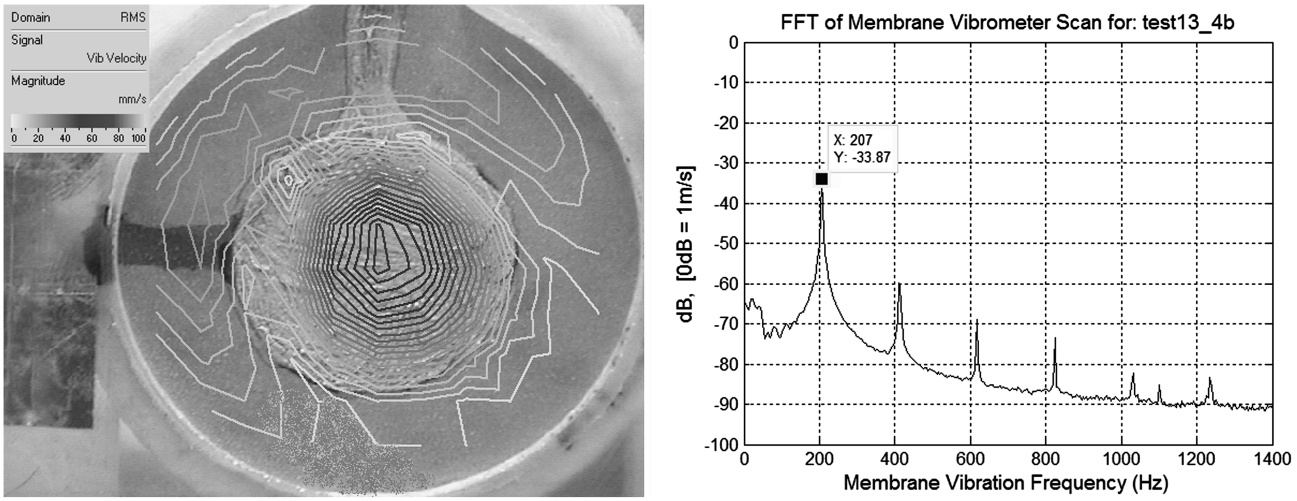

Fig. A26 Vibrometer scan at the second detected resonant frequency at 206 Hz excitation and 207 Hz vibration with a maximum rms vibrational velocity of 0.099 m/s at the center.

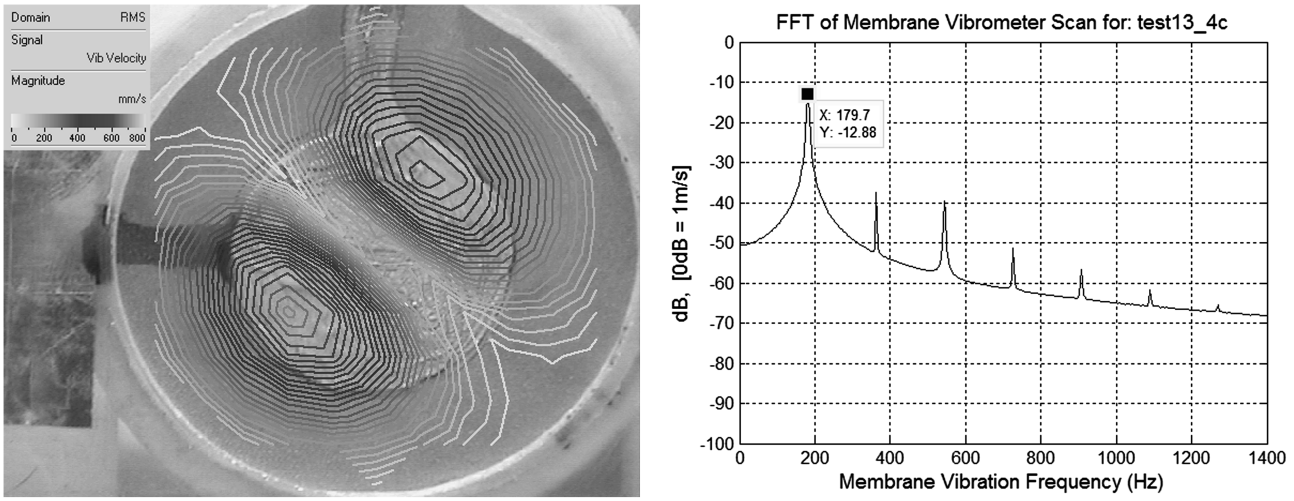

Fig. A27 Vibrometer scan at the third detected resonant frequency at 363 Hz excitation and 179.7 Hz vibration with a maximum rms vibrational velocity of 0.718 m/s.

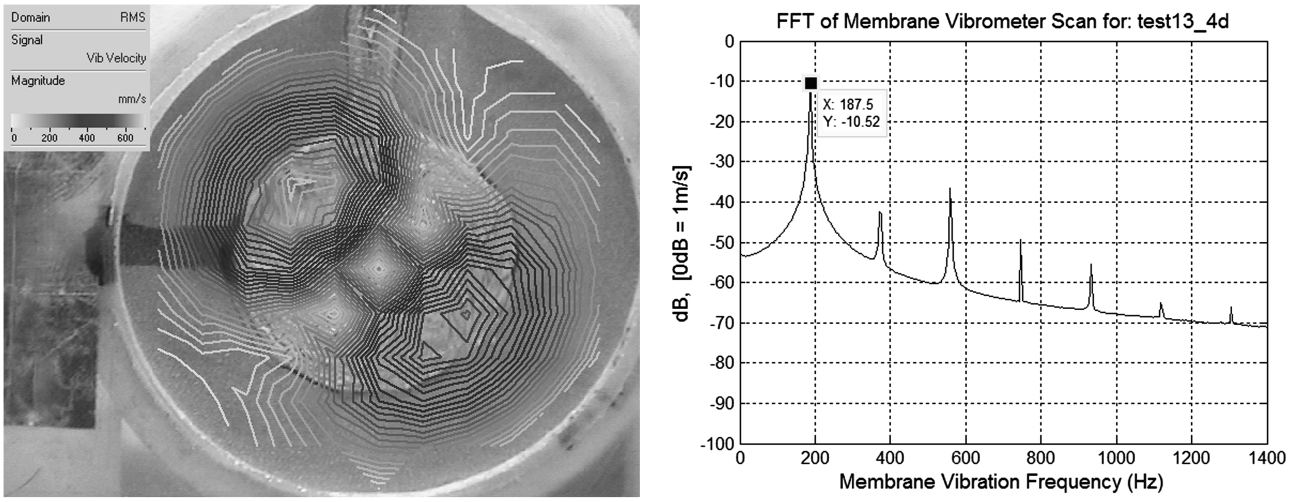

Fig. A28 Vibrometer scan at the fourth detected resonant frequency at 373 Hz excitation and 187.5 Hz vibration with a maximum rms vibrational velocity of 0.696 m/s.

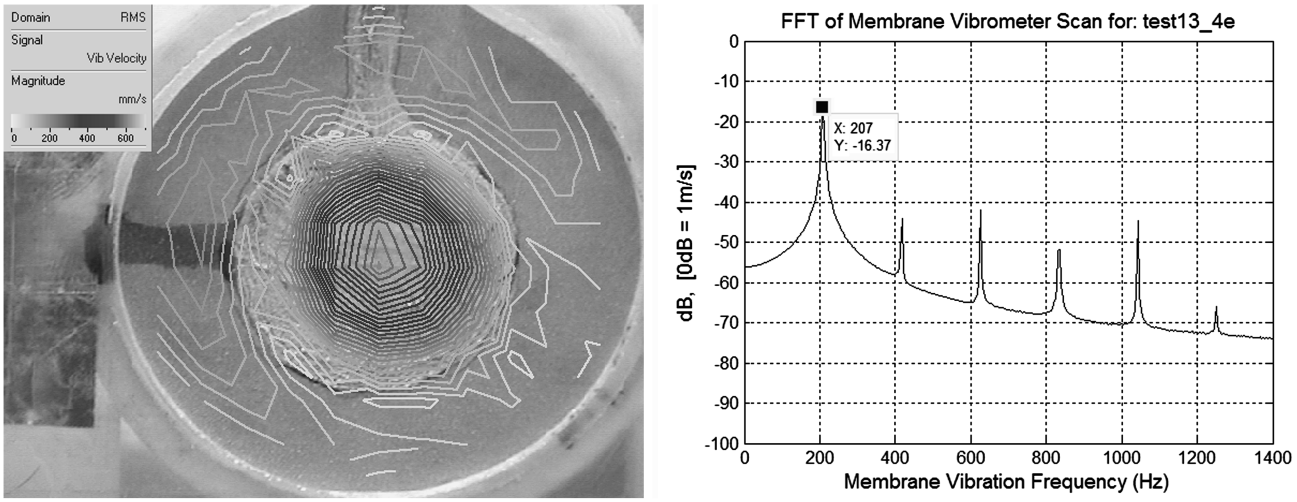

Fig. A29 Vibrometer scan at the fifth detected resonant frequency at 417 Hz excitation and 207 Hz vibration with a maximum rms vibrational velocity of 0.621 m/s at the center.

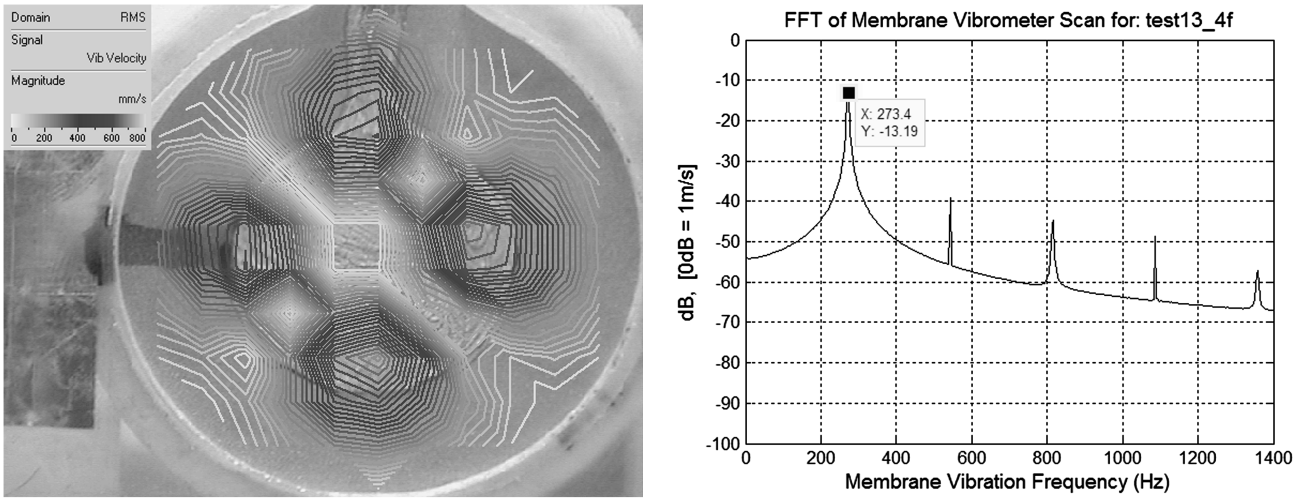

Fig. A30 Vibrometer scan at the sixth detected resonant frequency at 543 Hz excitation and 273.4 Hz vibration with a maximum rms vibrational velocity of 0.721 m/s.

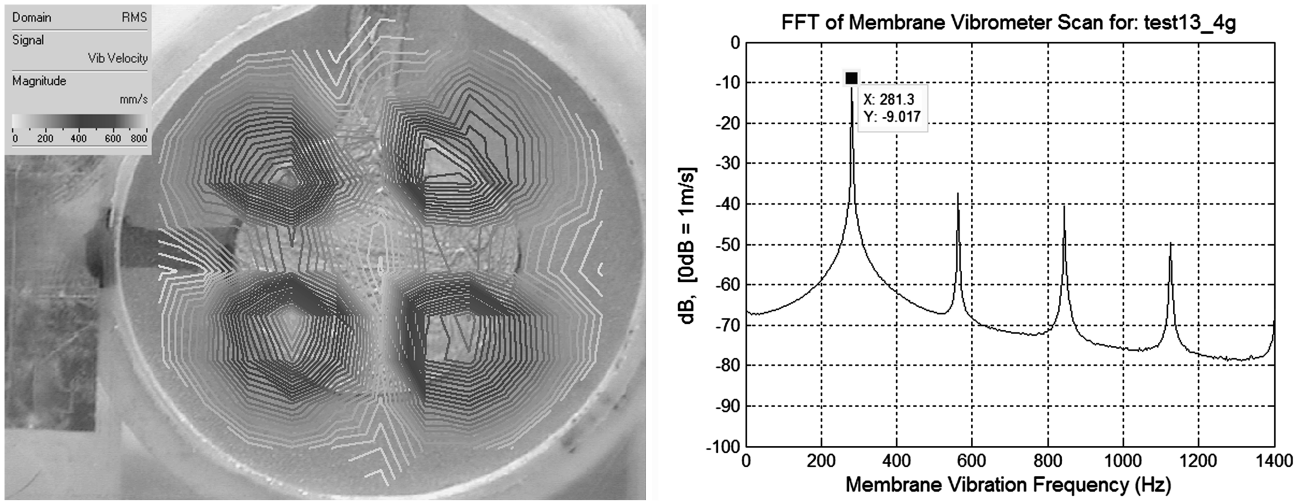

Fig. A31 Vibrometer scan at the seventh detected resonant frequency at 563 Hz excitation and 281.3 Hz vibration with a maximum rms vibrational velocity of 0.762 m/s.

Acknowledgments

The authors would like to acknowledge the funding secured by Norman Wereley of the University of Maryland, which made possible the acquisition of the scanning laser vibrometer used in this study. The authors would also like to thank Alison Flatau for providing the laboratory space in which the vibrometer experiments were performed at the University of Maryland and Joycelyn Harrison of NASA Langley's Advanced Materials and Processing Branch for providing the laboratory space in which we perform our daily research. Appreciation also goes to fellow Morpheus Laboratory

colleagues Sandra Ugrina, Nelson Guerreiro, Robyn Harmon, Jared Grauer, Benjamin Nickless, and David Billingsley for their continued support, guidance, and inspiration. Finally, the authors would like to thank all those who have performed, and who continue to perform, research in active flow control. Without their imagination, hard work, and inspiration to build upon, our world would be less interesting.

References

[1] Seifert, A., Darabi, A., and Wygnanski, I., "Delay of Airfoil Stall by Periodic Excitation," *Journal of Aircraft*, Vol. 33, No. 4, 1996, pp. 691–698. doi:10.2514/3.47003

[2] Gad-el-Hak, M., "Flow Control: The Future," *Journal of Aircraft*, Vol. 38, No. 3, 2001, pp. 402–418. doi:10.2514/2.2796

[3] Ugrina, S., "Experimental Analysis and Analytical Modeling of Synthetic Jet-Cross Flow Interactions," Ph.D. Dissertation, Aerospace Engineering Dept., Univ. of Maryland, College Park, MD, 2007.

[4] Haack, S., "Flow Control Using Plasma and Synthetic Jet Actuators on Bluff Bodies," M.S. Thesis, Aerospace Engineering Dept., Univ. of Maryland, College Park, MD, 2007.

[5] Glezer, A., Allen, M. G., Coe, D. J., Smith, B. L., Trautman, M. A., Wiltse, J. W., et al., "Synthetic Jet Actuator and Application Thereof," U.S. Patent 5,758,823, 1998.

[6] Prandtl, L., *Verhandlungen des Dritten Internationalen Mathematiker-Kongresses in Heidelberg 1904*, edited by A. Krazer, Teubner, Leipzig, Germany, 1905, p. 484; also *Early Developments of Modern Aerodynamics*, edited by J. A. K. Ackroyd, B. P. Axcell, and A. I. Ruban, Butterworth-Heinemann, Oxford, 2001, p. 77 (English translation).

[7] Hassan, A., and Munts, E., "Transverse and Near Tangent Synthetic Jets for Aerodynamic Flow Control," AIAA Paper 2000-4334, 2000.

[8] Smith, D., Amitay, M., Kibens, V., Parekh, D., and Glezer, A., "Modification of Lifting Body Aerodynamics using Synthetic Jet Actuators," AIAA Paper 98-209, 1998.

[9] McCormick, D., "Boundary Layer Separation Control with Directed Synthetic Jets," AIAA Paper 2000-0519, 2000.

[10] Gilarranz, J., and Rediniotis, O., "Compact, High-Power Synthetic Jet Actuators for Flow Separation Control," AIAA Paper 2001-0737, 2001.

[11] Seifert, A., and Pack, L., "Oscillatory Control of Separation at High Reynolds Numbers," *AIAA Journal*, Vol. 37, No. 9, Sept. 1999, pp. 1062–1071. doi:10.2514/2.834

[12] Chatlynne, E., Rumighy, N., Amitay, M., and Glezer, A., "Virtual Aero-Shaping of a Clark-Y Airfoil Using Synthetic Jet Actuators," AIAA Paper 2001-0732, 2001.

[13] Gilarranz, J. L., Traub, L. W., and Rediniotis, O. K., "Characterization of a Compact, High-Power Synthetic Jet Actuator for Flow Separation Control," AIAA Paper 2002-0127, 2002.

[14] Agashe, J. S., Arnold, D. P., and Cattafesta, L. N., "Development of Compact Electrodynamic Zero-Net Mass-Flux Actuators," AIAA Paper 2009-1308, 2009.

[15] Slipher, G. A., and Hubbard, J. E., "Description and Characterization of an Electroactive Polymer Synthetic Jet Actuator," *Electroactive Polymer Actuators and Devices (EAPAD)*, Proceedings of SPIE: The International Society for Optical Engineering, Vol. 6524, Society of Photo-Optical Instrumentation Engineers, Bellingham, WA, 2007, pp. 65240I.1–65240I.12.

[16] Gravatt, L., and Flatau, A., "Resonance Based Low Frequency Synthetic Jet Actuator Modeling, Design, and Testing," *Smart Structures and Integrated Systems*, Proceedings of SPIE: The International Society for Optical Engineering, Vol. 6173, Society of Photo-Optical Instrumentation Engineers, Bellingham, WA, 2006, pp. 61730L.1–61730L.10.

[17] Liang, Y., Kuga, Y., and Taya, M., "Design of Synthetic Jet Actuator Based on FSMA Composite," *Proceedings of SPIE*, Vol. 5762, Industrial and Commercial Applications of Smart Structures Technologies, 2005.

[18] Guy, Y., Mclaughlin, T. E., and Morrow, J. A., "Velocity Measurements in a Synthetic Jet," AIAA Paper 2001-118, 2001.

[19] Chen, F.-J., Yao, C., Beeler, G. B., Bryant, R. G., and Fox, R. L., "Development of Synthetic Jet Actuators for Active Flow Control at NASA Langley," AIAA Paper 2000-2405, 2000.

[20] Bailo, K. C., Brei, D. E., and Calkins, F. T., "Investigation of PVdF Active Diaphragms for Synthetic Jets," *Industrial and Commercial Applications of Smart Structures Technologies*, Proceedings of SPIE: The International Society for Optical Engineering, Vol. 3991, Society of Photo-Optical Instrumentation Engineers, Bellingham, WA, 2000, pp. 220–231.

[21] Smith, B. L., and Glezer, A., "Vectoring and Small-Scale Motions Effected in Free Shear Flows Using Synthetic Jet Actuators," AIAA Paper 1997-213, 1997.

[22] Jenkins, C. H. M., and Korde, U. A., "Membrane Vibration Experiments: An Historical Review and Recent Results," *Journal of Sound and Vibration*, Vol. 295, Apr. 2006, pp. 602–613. doi:10.1016/j.jsv.2006.01.036

[23] Lee, S., Kim, K. J., and Park, H. C., "Modeling of an IPMC Actuator-Driven Zero-Net-Mass-Flux Pump for Active Flow Control," *Journal of Intelligent Material Systems and Structures*, Vol. 17, June 2006, pp. 533–541. doi:10.1177/1045389X06058879

[24] Seeley, C. E., Uttukar, Y., and Arik, M., "Coupled Structural and Fluid Dynamics Modeling of a Synthetic Jet," AIAA Paper 2008-1880, 2008.

[25] Lin, X., Jiying, and Chen, Z., "Research on Terminal Behavior of Electrostatically Actuated Micropump Membrane Based on Modal Analysis," *Mechatronics, MEMS, and Smart Materials*, Proceedings of SPIE: The International Society for Optical Engineering, Vol. 6040, Society of Photo-Optical Instrumentation Engineers, Bellingham, WA, 2005, pp. 60400U.1–60400U.6.

[26] Pack, L. G., and Seifert, A., "Multiple Mode Actuation of a Turbulent Jet," AIAA Paper 2001-735, 2001.

[27] Gallas, Q., Holman, R., Nishida, T., Carroll, B., Sheplak, M., and Cattafesta, L., "Lumped Element Modeling of Piezoelectric-Driven Synthetic Jet Actuators," *AIAA Journal*, Vol. 41, No. 2, Feb. 2003, pp. 240–247. doi:10.2514/2.1936

[28] Gallas, Q., "On the Modeling and Design of Zero-Net Mass Flux Actuators," Ph.D. Dissertation, Univ. of Florida, Gainesville, FL, 2005.

[29] Muller, M. O., Bernal, L. P., Washabaugh, P. D., Kim, H. S., and Najafi, K., "Resonance Effects of Electrostatically Actuated Acoustic Jets," AIAA Paper 2003-1272, 2003.

[30] Ugrina, S., and Flatau, A., "Investigation of Synthetic Jet Actuator Design Parameters," *Smart Structures and Integrated Systems*, Proceedings of SPIE: The International Society for Optical Engineering, Vol. 5390, Society of Photo-Optical Instrumentation Engineers, Bellingham, WA, 2004.

[31] Arunajatesan, S., Oyarzun, M., Palaviccini, M., and Cattafesta, L., "Modeling of Zero-Net Mass-Flux Actuators for Feedback Flow Control," AIAA Paper 2009-743, 2009.

[32] Rusovici, R., and Lesieutre, G. A., "Design of a Single-Crystal Piezoceramic-Driven Synthetic Jet Actuator," *Smart Structures and Integrated Systems*, Proceedings of SPIE: The International Society for Optical Engineering, Vol. 5390, Society of Photo-Optical Instrumentation Engineers, Bellingham, WA, 2004, pp. 276–283.

[33] Ro, J., and Wu, K. C., "Finite Element Analysis and Performance Evaluation of Synthetic Jet Actuators," *Smart Structures, Devices, and Systems*, Proceedings of SPIE: The International Society for Optical Engineering, Vol. 4935, Society of Photo-Optical Instrumentation Engineers, Bellingham, WA, 2002, pp. 101–112.

[34] Crook, A., Sadri, A. M., and Wood, N. J., "The Development and Implementation of Synthetic Jets for the Control of Separated Flow," AIAA Paper 1999-3176, 1999.

[35] Cattafesta, L., Mathew, J., and Kurdila, A., "Modeling and Design of Piezoelectric Actuators for Fluid Flow Control," AIAA Paper 2000-5534, 2000.

[36] Slipher, G. A., Hubbard, J. E., and Flatau, A. B., Univ. of Maryland, College Park, MD, U.S. Patent Application 60/828,880 for "Electroactive Polymer-Based Synthetic Jet Actuator Design," Oct. 2006.

[37] Thomas, R., "EAPs: From New Microactuators to Artificial Muscle," SRI Consulting Business Intelligence, Menlo Park, CA, June 2006.

[38] Pelrine, R., Kornbluh, R., Pei, Q., and Joseph, J., "High-Speed Electrically Actuated Elastomers with Strain Greater Than 100%," *Science*, Vol. 287, No. 54542000, pp. 836–839. doi:10.1126/science.287.5454.836

[39] Choi, H. R., Kwangmok, J., Chuc, N. H., Jung, M., Koo, I., Koo, J., et al., "Effects of Prestrain on Behavior of Dielectric Elastomer Actuator," *Electroactive Polymer Actuators and Devices (EAPAD)*, Proceedings of SPIE: The International Society for Optical Engineering, Vol. 5759, Society of Photo-Optical Instrumentation Engineers, Bellingham, WA, 2005, pp. 283–291.

[40] *Model Design Manual*, McDonnell Douglas Engineering Dept., Model Design Group, Long Beach, CA, Dec. 1981.

[41] Jabareen, M., and Eisenberger, M., "Free Vibrations of Non-Homogeneous Circular and Annular Membranes," *Journal of Sound and Vibration*, Vol. 240, 2001, pp. 409–429. doi:10.1006/jsvi.2000.3249

R. Ohayon
Associate Editor